CHALMERS
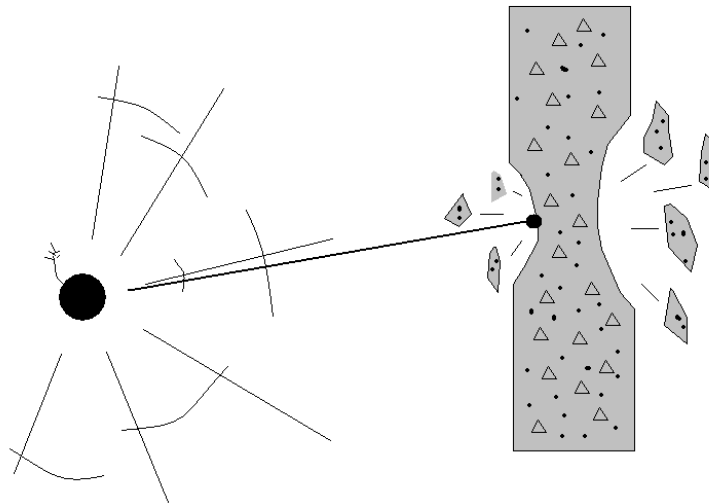
Concrete wall subjected to fragment impacts

Numerical analyses of perforation and scabbing

RASMUS REMPLING

Department of Structural Engineering and Mechanics
Concrete Structures

CHALMERS UNIVERSITY OF TECHNOLOGY

Göteborg, Sweden 2004

MASTER THESIS 04:1

Concrete wall subjected to fragment impacts

Numerical analyses of perforation and scabbing

RASMUS REMPLING

Department of Structural Engineering

Concrete Structures

CHALMERS UNIVERSITY OF TECHNOLOGY

Göteborg, Sweden 2004

Concrete wall subjected to fragment impacts

Numerical analyses of perforation and scabbing

RASMUS REMPLING

Concrete wall subjected to fragment impacts

Numerical analyses of perforation and scabbing

RASMUS REMPLING

Department of Structural Engineering and Mechanics

Concrete Structures

Chalmers University of Technology

ABSTRACT

Concrete subjected to fragment impact is mainly related to protective structures such as civil defence shelters where the main threat arise from explosions caused by military weapons.

For analysing impacts on concrete, material models are used in numerical analyses to simulate the reality. Such a model is the RHT model which is used to describe the material behaviour of concrete in the software Autodyn. The model has been evaluated for constructions subjected to compression and the result were satisfying. However, the function of the model is not satisfying for constructions subjected to tensile stresses. Therefore there exists a need for deepening the knowledge about penetration and scabbing of concrete subjected to fragment impact, about the parameters involved, and how the impact should be modelled in a accurate way.

The intentions are to give recommendations on how scabbing and perforation by fragment impact will be modelled in Autodyn. The numerical calculations, based on the RHT model, were verified by results of already performed full-scale tests. The model was calibrated from information gained from a parameter study of the most important parameters such as tensile strength, softening energies, strain rate and shear strength.

It was found out that by a calibration of the parameters conduction strain rate and shear resistance, in the material model, a result was obtained that was in accordance with the full-scale tests at the backside of the specimen. On the front side the result was not that convincing but showed tendencies that with further evaluation of the material model it could reach satisfaction.

Key words: concrete, fragment, blast, projectile, impact, penetration, perforation, scabbing, dynamic loading, dynamic resistance, strain rate, numerical analysis, protective structures.

Betongvägg utsatt för splitterbelastning
Numeriska analyser av genomträngning och utstötning

RASMUS REMPLING

Institutionen för konstruktion och mekanik
Betongbyggnad

Chalmers tekniska högskola

SAMMANFATTNING

Splitter belastad betong återfinns nästan uteslutande i skyddande konstruktioner såsom skyddsrum. Det huvudsakliga hotet mot sådana konstruktioner är konventionella bomber som skapar splitter när de exploderar.

För att analysera splitter som träffar en betong konstruktion används material modeller i kombination med numeriska analyser. RHT modellen som använd i programvaran Autodyn är en sådan material modell. Modellen fungerar tillfredsställande för konstruktioner som är utsatta för tryck enligt tidigare utförda studier. För konstruktioner som är utsatta för drag har det visat sig att modellen inte ger tillfredsställande resultat, varpå det uppstått ett behov av en fördjupande studie utav genomträngning och utstötning på splitter belastad betong.

Arbetes intention är att ge rekommendationer om hur utstötning och genomträngning bör modelleras i Autodyn vilket förutsätter en fungerande material modell. Modellen har verifierats med resultat från tidigare utförda försök där en SKF kula sköts på betong. Före verifieringen kalibrerades modellen utifrån en parameterstudie av de viktigaste parametrarna, drag hållfasthet, brottenergi, töjningshastighet och skjuvhållfasthet.

Resultatet blev att det var möjligt att kalibrera parametrarna som styr töjningshastighet och skjuvhållfasthet så att ett överensstämmande resultat med de fullskaliga försöken uppnås, men endast på baksidan av provet. På framsidan, ingångssidan, var resultatet inte lika övertygande men visade tendenser till att kunna bli bättre med en djupare studie an material modellen.

Nyckelord: betong, splitter, penetration, genomträngning, utstötning, dynamisk belastning, dynamisk hållfasthet, töjningshastighet, numeriska analyser, skyddskonstruktioner.

Contents

Appendix A: Calibration of variables.

Appendix B: Material model steel.

Appendix C: Attard model.

Appendix D: Analysis from calibration of parameters.

Preface

This master thesis have been carried out at the department of Structural Engineering and Mechanics, Chalmers University of Technology, as a final step in the Master Program Structural Engineering and Design during the summer and autumn of 2003. The examiner is Professor Kent Gylltoft.

I am very grateful for the rewarding work that my supervisor Joosef Leppänen has conducted giving me day-to-day consultancy and for being patient with all my questions. I also want to thank Björn Engstöm not only for his inspiring lectures in the basic course of concrete, at University of Chalmers, initiating my interest for concrete structures but also for his never ending ambitions to give the best lectures, which motivate and inspire the students to do their best.

And, finally, I want to show my appreciation to my life mentor and mother Margareta.

Göteborg, December 2003

Rasmus Rempling

Notations

Roman upper case letters

A	Area.
B	Parameter conducting residual strength.
C	Concrete class.
D	Parameter conducting strain rate.
D_e	Ingoing crater diameter.
D_s	Outgoing crater diameter.
D_1	Damage constant.
D_2	Damage constant.
D_3	Parameter for $Y_{fractured}$.
E_{ci}	Elasticity modulus, concrete.
E_{c0}	Constant calculating elasticity modulus, concrete.
E_0	Internal energy.
E_1	Internal energy.
F_{cap}	Parameter in Autodyn.
F_p	Internal pore pressure.
F_{RATE}	Parameter in Autodyn.
F_{st}	Counteracting force inside pore.
G	Shear modulus.
G_f	Fracture energy, Crack energy.
$G_{elastic}$	Parameter in Autodyn.
$G_{plastic}$	Parameter in Autodyn.
L	Length.
M	Parameter in Autodyn.
N	Parameter in Yield surface.
P	Pressure.

P^*	Pressure.
P_0	Pressure.
R_3	Parameter in Autodyn.
U_s	Velocity.
U_p	Velocity.
V	Volume.
V_0	Volume.
Y	Yield surface.
$Y_{elastic}$	Elastic stress.
Y_{fail}	Failure stress.
$Y_{residual}$	Residual stress.
Y^*_{res}	Residual strength.
Y_{txc}	Parameter in Autodyn.

Roman lower case letters

de/dt	Strain rate.
Δh_p	Change in pore diameter.
f_c	Concrete compressive strength.
$f_{c,imp}$	Impacting compressive strength.
f_{ck}	Characteristic compressive strength.
f_{ck0}	Constant for calculating compressive strength.
f_{cm}	Mean compressive strength after 28 days.
$f_{cm,cyl}$	Compressive strength, cylinder standard.
$f_{ctk0,m}$	Constant for calculating mean tensile stress.
$f_{ctm,imp}$	Impacting mean tensile strength.
f_{ctm}	Mean tensile strength.
f_t	Tensile strength.
f_s	Shear force.
h_p	Initial pore diameter.

p_e	Ingoing crater deepness.
p_s	Outgoing crater deepness.
t	Time.
w	Deformation.

Greek letters

ΔL	Increase in strength.
$\Delta \varepsilon_{pl}$	Change in plastic strain over time.
ε	Strain.
ε_c	Concrete strain.
$\dot{\varepsilon}$	Strain rate.
$\dot{\varepsilon}_0$	Constant for calculating strain rate.
$\dot{\varepsilon}_{ct}$	Concrete strain rate.
$\dot{\varepsilon}_{ct,0}$	Constant to calculate dynamic tensile strength.
$\varepsilon_p^{failure}$	Change in plastic strain over time.
μ	Deformation.
ν	Poissons ratio.
ρ	Density.
ρ_0	Initial density.
σ	Stress.
σ_c	Concrete Stress.
σ_{eq}	Actual Stress.
σ_{lat1}	Lateral pressure.
σ_{lat2}	Lateral pressure.
σ_{lat3}	Lateral pressure.
σ_y	Yield stress.
σ_1	Principal stress.

σ_2 Principal stress.

σ_3 Principal stress.

τ Shear resistance.

θ Meridian stress.

1 Introduction.

This master's thesis evaluate and explore the response of concrete subjected to fragment perforation and penetration by using numerical methods. The software Autodyn was used in the numerical analyses.

Concrete subjected to fragment impact is mainly related to protective structures such as civil defence shelters where the main threat arise from explosions caused by military weapons.

Civil defence shelters exposed to explosions are not only subjected to fragment impact. By the explosion follows a blast wave, falling debris from collapsing building, and fragment impact. The fragments impacting the construction penetrate or even may perforate the construction wall causing damage in the total height of the wall. Almost all penetrations that is fairly deep causes scabbing on the backside of the construction wall, generated by high tensile stresses.

In earlier projects at Chalmers University of Technology non-linear analysis have been performed by Johansson (1999) and Johansson (2000), analysing the blast wave and falling debris arisen from the explosion. These studies were followed by a study of the combination of blast wave and fragment impact, Leppänen (2002). However, the numerical analysis in Leppänen was limited to projectile penetrations. As a continuation, the ongoing research project by Leppänen involves also fragment perforations. This project is supposed to make a base for the study of the phenomenon related to the fragment penetrations of concrete.

For analysing impacts on concrete, material models are used in numerical analysis to simulate the reality. The RHT-model, applied in Autodyn, is used to describe the material behaviour of concrete. The model works properly for constructions subjected to compression. For constructions subjected to tensile stresses, however, is the function of the model not satisfying. Therefore there exists a need for deeper knowledge about penetration and scabbing of concrete subjected to fragment impact, about the parameters involved and how the impact should be modelled in a correct way.

The final goal is to give recommendations on how scabbing and perforation by fragment impact will be modelled in Autodyn. The goal should be reached by numerical calculations verified by results of already performed full scale tests and a parameter study of the most important parameters such as tensile strength, softening energies, strain rate and shear strength.

The method chosen, verifying the calibrated model, based on a parameter study with full-scale experiments is a fast method reaching results early in the process. As the experiments already are conducted the method also becomes cheap. An alternative method could be to calibrate and validate the model with test made in a laboratory and then apply the model to real structures. Such a method should take long time since every parameter have to be calibrated and validated and is therefore not suitable for a master thesis.

2 Response of concrete under dynamic loading.

The response of concrete under dynamic loading is not the same as for concrete under static loading mainly because of the high strain rates that are present for dynamic loading.

2.1 Response of concrete under static loading.

The response of concrete under static loading is known through the stress-strain relationship. The concrete under compression got an elastic response before the first crack develops as a result of tensile splitting. Tensile splitting is a result of the materials need of expansion perpendicular to the load axis. The first stage, in the concrete response, is correctly approximated with a linear response. The following stage in which the tensile splitting increases and further cracks develops the response is non-linear. While in the ultimate stage when failure occurs and the maximum capacity is reached, the increase in stress stops but the increase in deformation continues with a relaxation of stress continuing until the residual strength is reached. The residual strength is the strength that the member can produce after cracking because of the friction in the crack plane. However, in the uniaxial loading there is no residual strength. Concrete under tensile stress behaves more or less the same as under compressive stress but with the big difference that the tensile stress drops fairly quickly after the maximum stress is reached and cracking occurs, called tensile softening. The ultimate tensile strength is known to be less than one tenth of the ultimate compressive strength for normal strength concrete. There is no residual strength in a member loaded in tension.
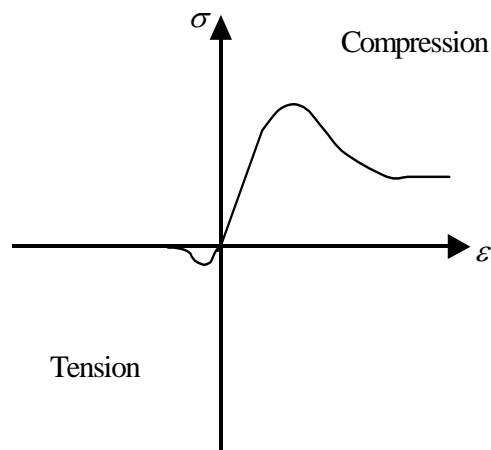

Figure 1: Stress strain relationship for concrete.

The expansion of the crack after it is initiated is governed by the amount of energy that needs to be released. This energy is called the fracture energy and is normally used as parameter in numerical analysis of concrete to control the crack development.
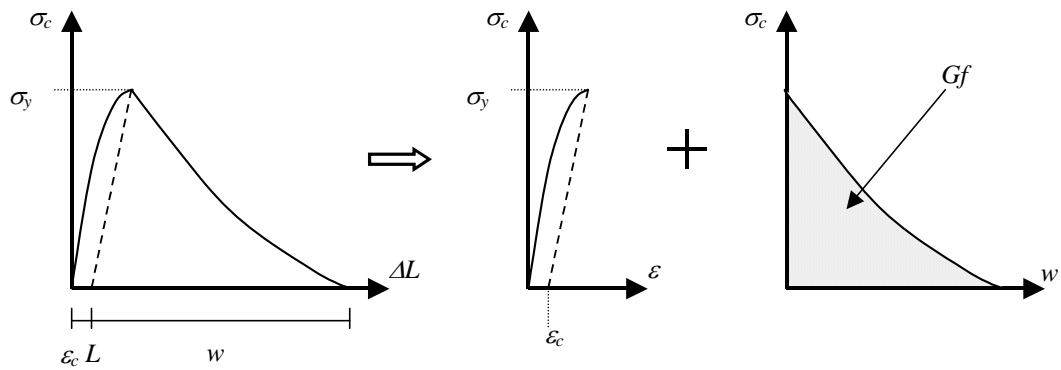
Figure 2: The displacement is divided into a stress-strain relationship and a stress crack width relation. The area under stress crack width is the fracture energy G_f.

When discussing the response of materials looking only in one direction, a simplification often is made to help the understanding. Unfortunately is the response dependent on all directions i.e. the loads and the material structure in three dimensions. A general stress state in three dimensions is described in a right angle system of coordinates with the normal stresses $\sigma_x, \sigma_y, \sigma_z$ and the shear stresses τ_x, τ_y, τ_z oriented according to Figure 3. In a certain position the stresses occur only as normal stresses, which are named the principal stresses $\sigma_1, \sigma_2, \sigma_3$.
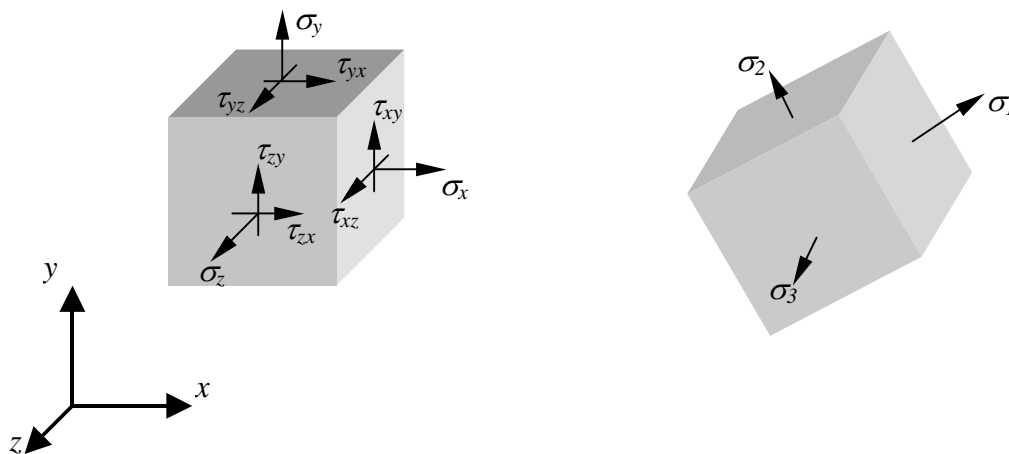

Figure 3: General stress state and principal stresses.

In uniaxial pressure, no lateral pressure, failure occurs as a combination of tensile splitting and shear failure, something that results in a quick descending curve. For confined concrete, i.e. concrete exposed to compression and lateral pressure, the descending curve is not that steep, as it tends toward the residual strength because of the fact that the confinement work against the tensile splitting. Another effect of lateral pressure is that the strength and stiffness increase and the strains are enlarged. While under tension and lateral pressure the strength is not highly affected but the strains are extended.
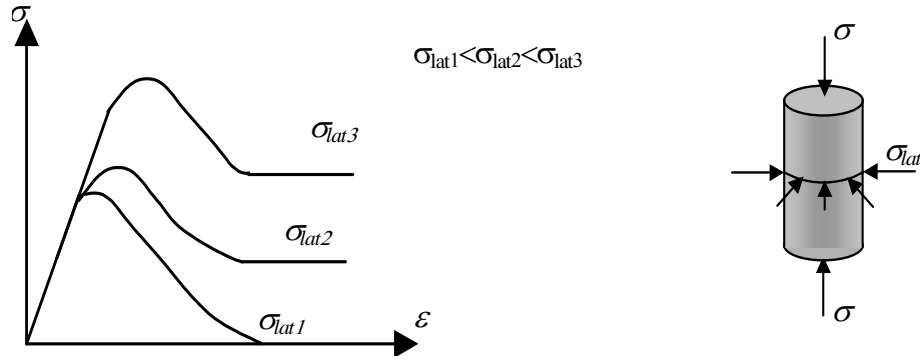
Figure 4: Effect of confinement.

2.2 Strain rate effect on the strength of concrete

It is known that the compressive and tensile strength increase with the strain rate i.e. strain rate is the velocity of the loading. Different test have been done looking at different parameters involved and consequently the shape of the strain rate-strength relationship of tensile strength and compressive strength deviate from each other, seen in Figure 5. The increase in strength with strain rate is divided into two parts. The first part considers lower strain rates and depends on the water content while the second part considers higher strain rates and is related to forces of inertia. In the CEB (1990) strain-strength relations are defined for both compression and tension, evaluated from the compressive strength of the material in the whole spectra (equation 2.4 and 2.8).

Tensile strength:

$$\frac{f_{ct,imp}}{f_{ctm}} = \left(\frac{\dot{\varepsilon}_{ct}}{\dot{\varepsilon}_{ct0}}\right)^{1,016*\delta_s} \quad \text{for } \left|\dot{\varepsilon}_{ct}\right| < 30 \text{ s}^{-1} \tag{2.1}$$

$$\frac{f_{ct,imp}}{f_{ctm}} = \beta_s * \left(\frac{\dot{\varepsilon}_{ct}}{\dot{\varepsilon}_{ct0}}\right)^{\frac{1}{3}} \quad \text{for } \left|\dot{\varepsilon}_{ct}\right| > 30 \text{ s}^{-1} \tag{2.2}$$

$$\log \beta_s = 7{,}11 * \delta_s - 2{,}33 \tag{2.3}$$

$$\delta_s = \frac{1}{10 + 6 \, f_{cm}\big/f_{cm0}} \tag{2.4}$$

Compressive strength:

$$\frac{f_{c,imp}}{f_{cm}} = \left(\frac{\dot{\varepsilon}_c}{\dot{\varepsilon}_{c0}}\right)^{1,026*\alpha_s} \quad \text{for } \left|\dot{\varepsilon}_c\right| < 30 \text{ s}^{-1} \tag{2.5}$$

$$\frac{f_{c,imp}}{f_{cm}} = \gamma_s * \left(\frac{\dot{\varepsilon}_c}{\dot{\varepsilon}_{c0}}\right)^{\frac{1}{3}} \quad \text{for } \left|\dot{\varepsilon}_c\right| > 30 \text{ s}^{-1} \tag{2.6}$$

$$\log \gamma_s = 6{,}156 * \gamma_s - 2 \tag{2.7}$$

$$\alpha_s = \frac{1}{5 + 9\,f_{cm}/f_{cm0}} \tag{2.8}$$

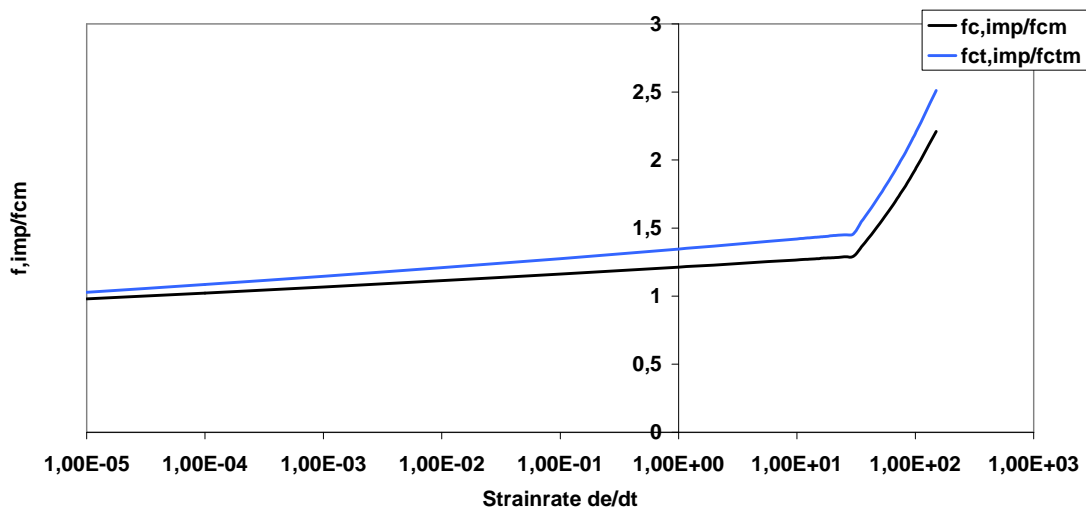**Strainrate effects on Compressive and Tensile strength**

Figure 5: Strain rate effects on the compressive and tensile strength.

It is seen in the formulas (equation 2.1-2.8) and the related graph (Figure 5) that both the compressive and the tensile strength increase with the strain rate. This phenomenon is very present and applicable when dealing with explosive loads, why it is relevant to explain the phenomenon in this report.

As the strength increase with the strain rate in the high strain rate range the nonlinarity of concrete decrease, which is explained by Zielinski (1981) as a result of the differences in the crack development. At lower strain rates the cracks are able to find the path that involve least energy. While at high strain rate the cracks take in a way a straighter path through the concrete and thus not only in the cement, as with static loading but also through the aggregate of the concrete. The higher strength of the aggregate explains consequently the increase of the compressive/tensile strength with increased strain rate.

At the lower strain rate range the strain rate effects are explained by another phenomenon. Rossi (1991) tries to explain the strength increasing effect by the free water effect in the material. Because of the random direction of the pores in the

concrete, Rossi (1991) chooses to only threat pores that are loaded perpendicular or parallel with their own direction.

For pores loaded perpendicular to its own direction Rossi (1991) and Han (1991) propose the same discussion as Kaplan (1980), to explain the alteration in compressive strength with increased strain rate and free water content. Han explains the alteration in compression strength by the fact that when concrete is compressed the water filled pores in the concrete want to close and consequently wants the free water to move from its initial location. Because of the viscosity of water and the fact that a bigger mass needs a bigger force to accelerate, the closing of the cell causes an internal pressure F_p, dependent on the size of the pore, the water content in the pore and the speed of the compression. This alteration in pressure counteracts the compression and an increase in compression strength is gained.
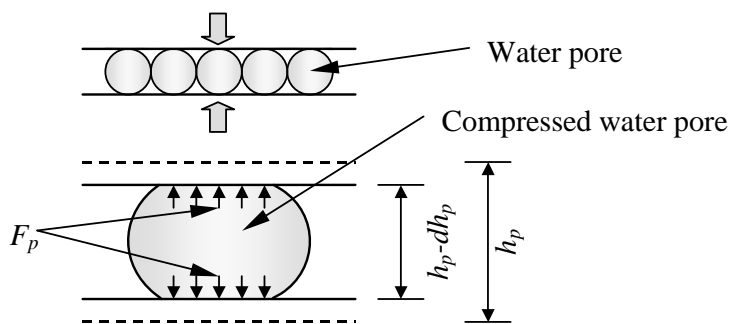

Figure 6: Pore water pressure.

Rossi (1991) proposes a physical mechanism capable of explaining the experimentally observed results, that pores loaded parallel with its own direction have an effect on the increased tensile strength with strain rate. Rossi explains the phenomenon by the Stefan effect. That the existence of a thin viscous film like water between two perfectly parallel plates, separated by a distance, causes a counteracting force F_{st} when the two plates are separated. In the same way as a plate of glass is difficult to lift when placed on a wet surface. Greater separating force generates a greater opposing force.
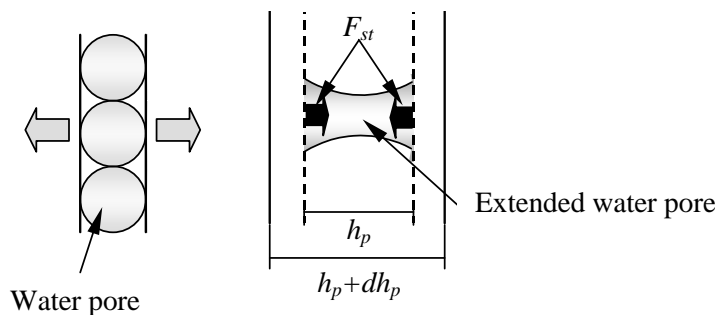

Figure 7: Stefan effect.

Concluding these hypotheses, it should be possible to say that the two effects are working together because of the general accepted theory that a compressed body in one direction wants to increase in its perpendicular direction and therefore should the two strength-increasing effects be present at the same time.

2.3 Strain rate effects considered in Autodyn.

Autodyn considers the increase in strength with strain rate in its numerical analysis by a factor called *Frate*. The factor *Frate* depends on the actual strain velocity and a basic value powered by a user defined parameter, one for compression and one for tension. As seen below are the function in Autodyn the same as CEB apply presented in equation (2.2) and (2.6) with the slight difference that the formulas follows different limits. The CEB uses the strain rate to set the limits while Autodyn uses the actual pressure.

$$Frate= \begin{cases} \left(\dfrac{\dot{\varepsilon}}{\dot{\varepsilon}_0} \right)^{\alpha} \text{ for } P > \frac{1}{3} f_c & \text{compression} & (2.9) \\ \\ \left(\dfrac{\dot{\varepsilon}}{\dot{\varepsilon}_0} \right)^{\delta} \text{ for } P < \frac{1}{3} f_t & \text{tension} & (2.10) \end{cases}$$

2.4 Stress waves.

As the report deals with penetration of a concrete wall is it in its place to explain the phenomenon of stress waves subjected to a material with free boundaries.

When the fragment comes in contact with the wall a stress wave is initiated. The stress wave propagates in the longitudinal and transverse directions and generates a compressive stress wave on its way. When the wave reach the border of the wall the wave is reflected and goes back generating tensional stresses equal to the compressive stresses but with opposite sign. Since the tensile strength is much lower than the compressive strength for concrete, scabbing could be caused by the high tensile stresses.
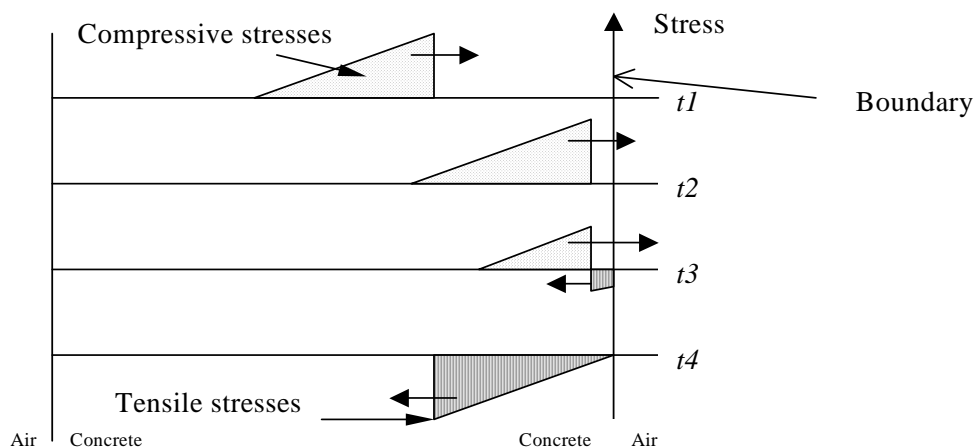

Figure 8: Stress wave development on a free boundary.

3 Numerical modelling of concrete under severe dynamic loading.

As described in the introduction one aim of the thesis is to give recommendations on how scabbing and perforation by fragment impact shall be modelled in Autodyn. Autodyn is a numerical solver for loading conditions of high strain rates and uses the standard methods for numerical modelling. It solves a wide range of non-linear problems in solid, fluid and gas dynamics by using numerical calculations. To describe the material movement it uses Lagrangian and Eulerian processors among others, described in chapter 3.2. The governing equations for numerical calculations in Autodyn are the Rankine-Hugoniot equations which treat conservation of mass, momentum, and energy described in chapter 3.1. To finish the description of the continuous changes without abruption called continuum. Two more relations, except load and boundary conditions, describing the material behaviour need to be explained. The two relations are the equation of state that describes the relationship between pressure and density, and a constitutive model which describes the material state related to pressure.

3.1 Conservation of mass, momentum and energy.

When the shock wave propagates through the media, built up by element-mesh in the model, it becomes compressed. The compression is exemplified by the deformation of the elements in the numerical calculations.

To describe the phenomenon a simile could be done. If we look at the compression of the material as a snowplough shovelling snow moving forward. If the snowplough moves with a velocity of U_p, the compressed snow in front of the plough moves with the same velocity U_p. On the other hand the region separating the compressed snow from the uncompressed, is moving with the velocity U_s which is greater than U_p, because of the fact that snow is added to the compressed region and the region border is so forth growing all the time. Meyers (1994) describes the phenomenon in a more scientific way so that it is possible to derive the governing equations. He chooses to simplify it by considering a cylinder, of unit cross-sectional area ($A=1$), which a piston penetrates.

Initially the piston, in Figure 9 is at rest, the media in the cylinder has before t_0 a pressure P_0, density ρ_0, velocity U_0, and an internal energy E_0. At the time t_0 the piston is pushed into the cylinder, with a velocity of U_p, compressing the material. After a time-step δt has the compressed region of the material moved forward a distance equal to $U_s * t_1$, U_s is the velocity at the end of the compressed region and $t_1 = t_0 + \delta t$, while the piston has moved a shorter distance equal to $U_p * t_1$. After conservation of mass, momentum and energy, i.e. keeping the properties from the undeformed region to the deformed region, another time-step takes place and the cycle is completed. Applying this theory to a finite element mesh with the compressed zone as an element changing in shape but keeping the same internal properties is reached by the governing equations.

With Figure 9 the equations of conservation of mass, momentum, and energy can be derived.

- Conservation of mass:

The mass of initial uncompressed material = The mass of the compressed material.

$$U_s t_1 A \rho_0 = \rho (U_s - U_p) t_1 A \qquad (3.1)$$

- Conservation of momentum:

The change of momentum (mass*velocity) = The impulse (F dt) of the external forces.

$$A(U_s - U_p) t_1 \rho U_p - 0 = (P - P_0) t_1 A \qquad (3.2)$$

- Conservation of energy:

The change in internal energy plus change in kinetic energy = The work done by the external forces.

Change in internal energy =

$$E_1 \lfloor \rho (U_s - U_p) t_1 A \rfloor - E_0 \lfloor \rho_0 U_s t_1 A \rfloor = (E_1 - E_0) \rho_0 U_s t_1 A \qquad (3.3)$$

Change in kinetic energy =

$$\tfrac{1}{2} \lfloor \rho (U_s - U_p) t_1 A \rfloor U_p^2 - 0 = \tfrac{1}{2} \rho_0 U_s t_1 A \qquad (3.4)$$

The work of the external forces =

$$PU_p t_1 A \qquad (3.5)$$

Equations (3.3) + (3.4) = (3.5) and yields:

$$\rightarrow (E_1 - E_0) \rho_0 U_s t_1 A + \tfrac{1}{2} \rho_0 U_s t_1 A U_p^2 = PU_p t_1 A \qquad (3.6)$$

Simplifications of the equations (3.1), (3.2) and (3.6) gives finally the conservation laws:

$$\rho_0 U_s = \rho (U_s - U_p) \qquad \text{mass} \qquad (3.7)$$

$$(U_s - U_p) \rho_0 U_p = P - P_0 \qquad \text{momentum} \qquad (3.8)$$

$$E - E_0 = \tfrac{1}{2} (P + P_0)(V_0 - V) \qquad \text{energy} \qquad (3.9)$$
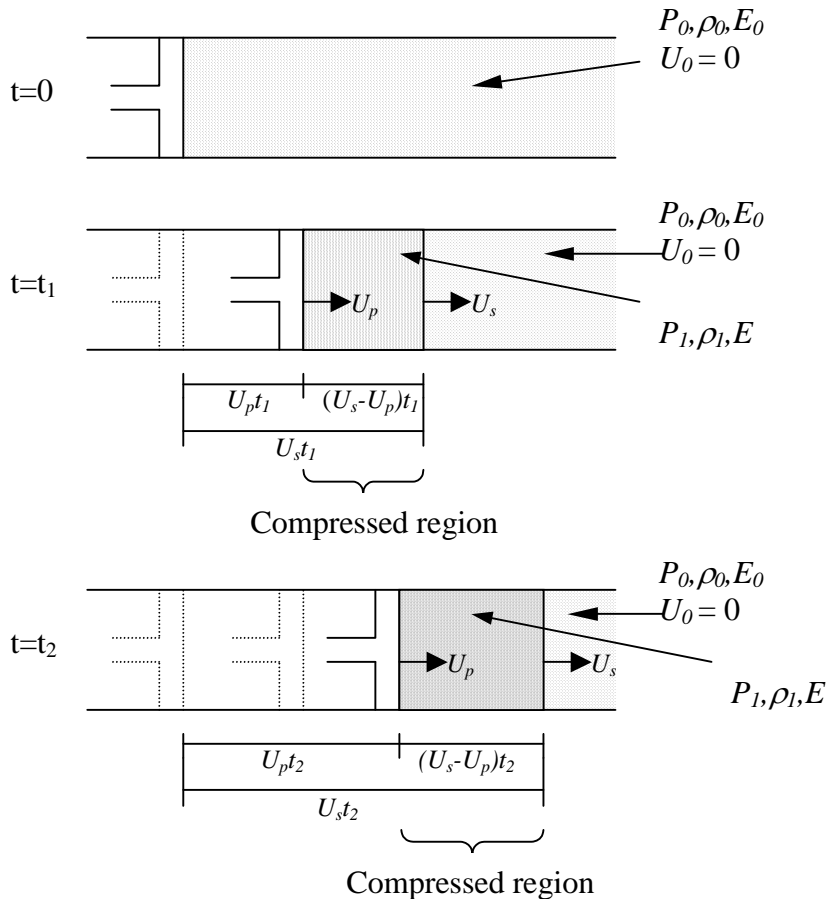
Figure 9: Piston penetrating a cylinder to simplify the derivation of the general equations.

3.2 Mesh techniques.

There exist two main processors for calculating with finite elements. One for modelling solid materials and structures named Lagrange and one for modelling fluid material and large distortions named Euler. The mesh in the Lagrange processor follows the material as it deforms and the material stays inside the initial element definition with no transport of material between elements. The advantage of this, according to the Autodyn manual tends to be that the computational process is fast. It is also seen that material interfaces, free surfaces, and history dependent material behaviour are easier to follow. The disadvantage of Lagrange is the inaccuracy and inefficient solution when the mesh becomes highly distorted by excessive material movement, which may lead to a termination of the calculation. Autodyn applies solutions such as rezoning and remapping of the distorted mesh to avoid this problem. Another way to overcome the problem is to use an erosion model that remove the element that has distorted more than a prescribed value, normally chosen as the plastic strains. The backlash with the erosion model technique is that it gives a non-physical solution by the fact that mass is removed from the system.
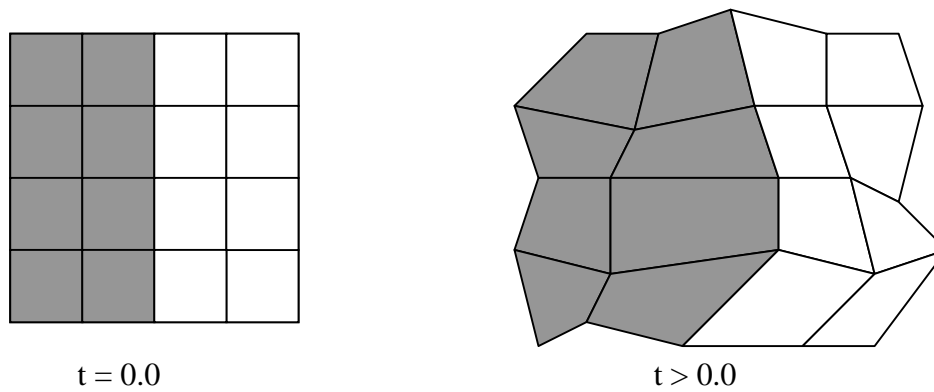
<center>t = 0.0   t > 0.0</center>

Figure 10: Lagrangian mesh distortion for one subgrid.

As the Euler processor have not been used in the analysis it will only be mentioned shortly. The processor uses a control volume method to solve the equations that govern conservation of mass, momentum, and energy. This is done with a two-step numerical procedure where the first is a normal Lagrange step followed by the Euler step. In the Euler step the updated variables are mapped onto the Euler mesh, i.e. the material moves inside the mesh.

3.3 Equation of state.

The general equations derived in chapter 3.1 are three but the number of unknowns is five. To be able to determine all parameters involved there is need for more equations. One of them is the equation of state (EOS) which relates the pressure to the internal energy and the density.

$$P = P(\rho, E) \tag{3.10}$$

For a static numerical analysis the EOS normally describes the material behaviour and is generally assumed to be linear, while for severe loading it is essential to take into account the non-linearity of the material behaviour because of the high hydrostatic pressure.

3.3.1 Concrete

For concrete it is known that the relationship pressure – density becomes non-linear at a certain pressure. Before this brake point the concrete response is elastic and thus linear. With increased loading the pores are compressed and micro cracking occurs as a consequence the pores collapse and the material becomes compacted. At very high pressure the concrete is fully compacted and the relationship between pressure and density once again become linear. In Figure 11 ρ_0 is defined as the initial undisturbed concrete density and ρ_s as the density of the fully compacted concrete at zero pressure. The material behaves elastic until it reaches a pressure P_{crush} where the plastic compaction phase is initiated.
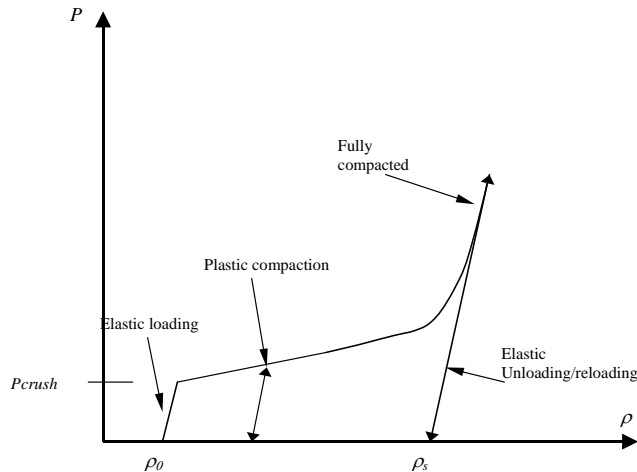
Figure 11: Equation of state (EOS), the relationship between pressure and density.

3.3.2 Steel

Steel in compression is more or less linear proportional to the hydrostatic pressure why it is essential to use a linear EOS for describing the behaviour of steel where the pressure level depends on the bulk modulus K and the compression μ as seen in Figure 12.
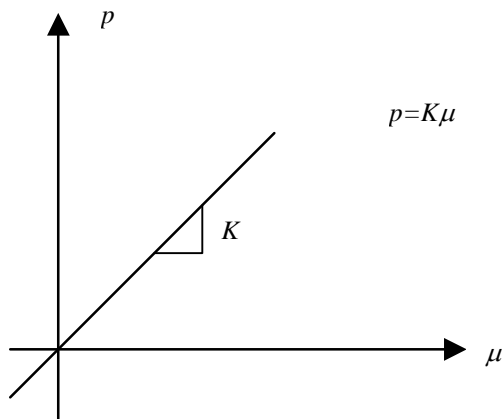

Figure 12: Equation of state for steel.

3.4 Constitutive models.

Another relationship that should be stated is the relationship that relates the stress to the strains (ε), strain rates ($\dot{\varepsilon}$), internal energy (E), and damage (D), which is done by the general form stated in equation (3.11).

$$\sigma_{ij} = f\left(\varepsilon_{ij}, \dot{\varepsilon}_{ij}, E, D\right) \qquad (3.11)$$

In Autodyn this relationship is defined with the RHT model by Riedel (2000) including pressure hardening, strain hardening, strain rate hardening, third invariant dependence (the product of the three principal stresses), and damage. Three pressure dependent surfaces; one defining failure, one that defines the elastic limit and one for the residual strength describe this.

In Figure 14 the RHT model is defined with yield strength over pressure, where the pressure is the mean value of the three principal stresses according to equation (3.12). When an element is exposed to pressure applied linear, line one and two in Figure 14, it start to strain with a following increase in stress, in the model this stress strain relationship, called the elastic phase continues with inclination according to the elasticity modulus until the elastic limit surface is reached. In next phase, called hardening phase, the non-linear response is approximated with a linear response with the inclination set by the parameters $G_{elastic}$ and $G_{plastic}$, equation (3.13) and Figure 13. The failure surface ends this phase and the softening phase starts. In the softening phase the pressure and the stress start to descend towards the residual surface according to equation (3.14) to (3.16) and the damage constants *D1* and *D2*. If the pressure is applied, with a lower angle, line two (still linear), a higher elastic and failure limit is reached as seen in the right picture in Figure 14. For the special pressure case when all the principal stresses are equal, the increase in pressure follows the x-axis in Figure 14 and is called hydrostatic pressure.

$$p = \frac{\sigma_1 + \sigma_2 + \sigma_3}{3} \qquad (3.12)$$

$$\varepsilon_{pl(pre-softening)} = \frac{Y_{fail} - Y_{elastic}}{3G} \left(\frac{G_{elastic}}{G_{elastic} - G_{plastic}} \right) \qquad (3.13)$$

with Y_{fail} and $Y_{elastic}$ according to Figure 14 and G as shear modulus.
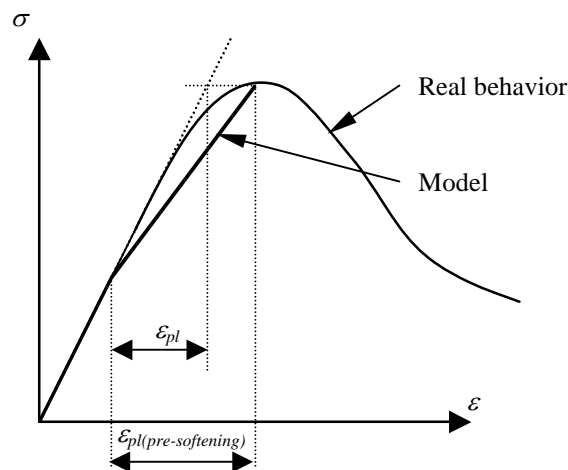

Figure 13: Hardening phase.

$$\varepsilon_p^{failure} = D_1 \left(P^* - P_{spall}^* \right)^{D_2} \qquad (3.14)$$

$$D_3 = \sum \frac{\Delta\varepsilon_{pl}}{\varepsilon_p^{failure}}$$ *(3.15)*

$$Y_{fractured} = (1 - D_3)Y_{fail} + D_3 Y_{residual}$$ *(3.16)*

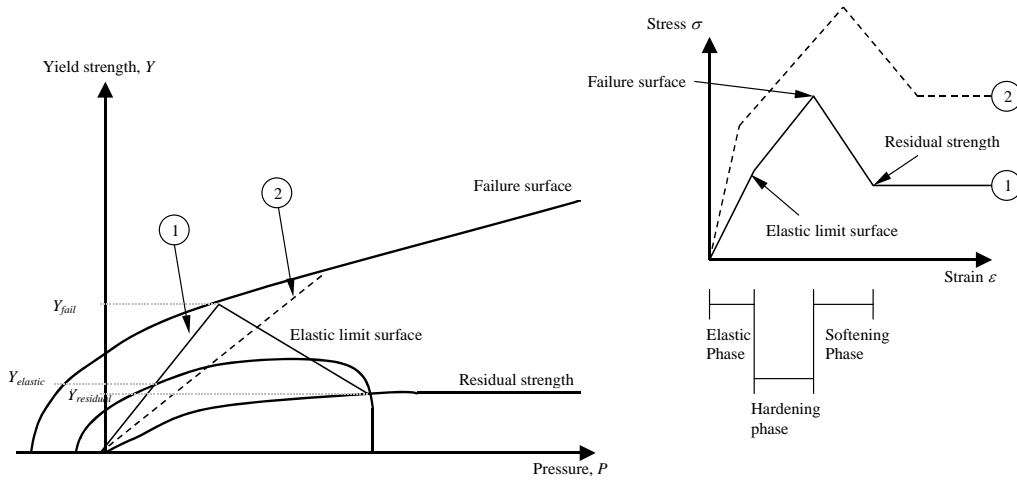with $Y_{residual}$ according to equation (3.18)

Figure 14: RHT model.

The failure surface is a function of pressure, the actual stress, the meridian ratio between tension / compression, and the strain rate.

$$f\left(P, \sigma_{eq.}, \theta, \dot{\varepsilon}\right)$$ *(3.17)*

The elastic surface is scaled in Autodyn from the failure surface by only two parameters.

The residual strength, defined by the parameters *B* and *M*, is a function of the pressure level.

$$Y_{res}^* = B * \left(P^*\right)^M$$ *(3.18)*

the fragments where made of steel and thus in the numerical analysis a perfect von Mises strength model was used, where the yield surface can be calculated from the second invariant $(\sigma_1\sigma_2 + \sigma_2\sigma_3 + \sigma_3\sigma_1)$ of the stresses.
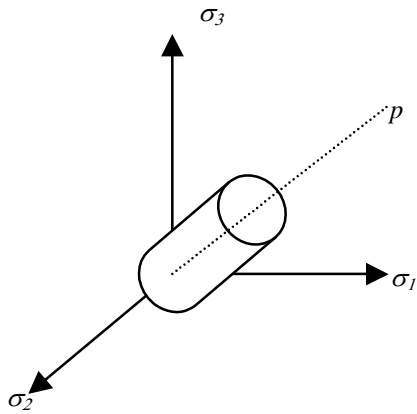
Figure 15: von Mises strength model.

3.5 Autodyn.

In Autodyn the materials, which are defined by the statements in chapter 3.4, are inserted in subgrids giving the model. The physical parts of the model define the subgrids and each part got its own mesh.

The Lagrange processor makes series of calculations in each timestep in every subgrid as shown in Figure 16. Starting with updating the boundaries and interactive forces and combining these with the forces from inner zones computed during the last cycle. From the momentum equation and integration, the velocities, accelerations, and positions are computed for every node. These values make it possible to calculate the zonal volumes and the strain rates. And finally the material model and the energy equation give the zonal pressure, stresses, and energies, which provide the forces for the next calculation cycle. For coupling subgrids together, the Lagrange processor uses interactive forces for the additional calculations needed.

Direct calculation

| Nodal Velocities & Displacements | | Zone Volumes & Strain rate |

Integration

Material Model

| Nodal Accelerations | | Zone Pressures and Stresses |

Force / Mass

Conservation of Momentum

| Nodal Forces |

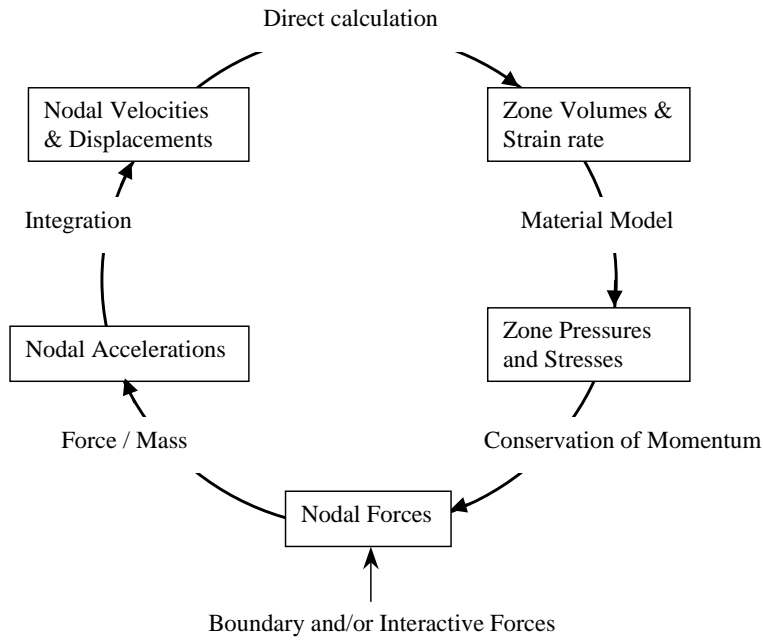Boundary and/or Interactive Forces

Figure 16: Lagrange computation cycle.

4 Numerical analysis of concrete perforation.

The thesis aims to predict perforation and scabbing of a fragment impacting a concrete wall by using numerical methods, therefore experimental results from FOA (Swedish defence institute of research) have been used to calibrate and verify the actual material model.

For calibrating and deepen the knowledge about the effect of the different parameters involved, a parameter study was carried out. From a reference analysis the parameters were changed and analysed. The effects of the changes, could be seen and a calibration of the material model where done.

Four different experimental series have been compared with numerical analysis. All experiments are loaded with the same type of fragment but with different velocities of the impacting fragment. In the experiments two different types of concrete have been used as well as three different thickness of the concrete wall.

4.1 Experimental series.

The experimental series used, have been carried out by the Swedish FOA and documented by Erkander, Pettersson (1985). The experiments are done by simulating warhead fragments with spherical and cylindrical projectiles fired against different types of concrete slabs such as ordinary concrete, cementbound shingle, fibre concrete and plain shingle. This report considers only ordinary concrete and study therefore only the experiments related to this. During the experiments the velocities of the impact, depth of penetration, and the impulse of the scabbed material were measured.

The experiments were performed, as visualized in Figure 17, with a velocity measuring unit, the sample that should be studied, and a verification board of wood to track the scabbed material.
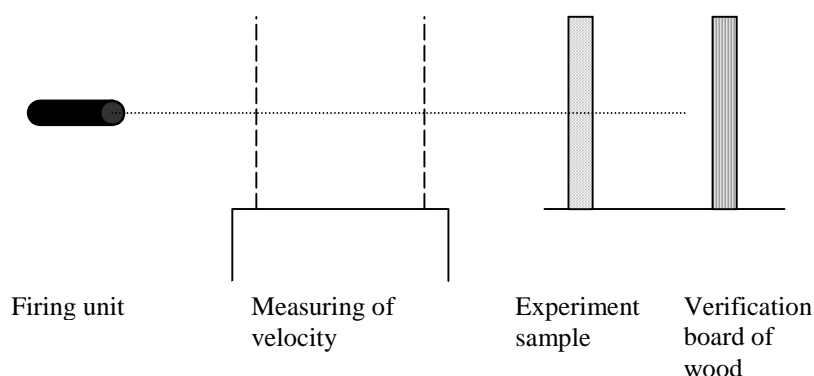

Firing unit   Measuring of velocity   Experiment sample   Verification board of wood

Figure 17: Arrangement of experiments.

Every experiment sample is a slab with an area of $100 * 100$ cm^2, made of the concrete qualities K60 or K25. Reinforced by K40 ϕ 10 placed in a pattern so that nine squares were obtained. This was done so that it was possible to fire up to nine times on one single slab without interference between the different fire series.
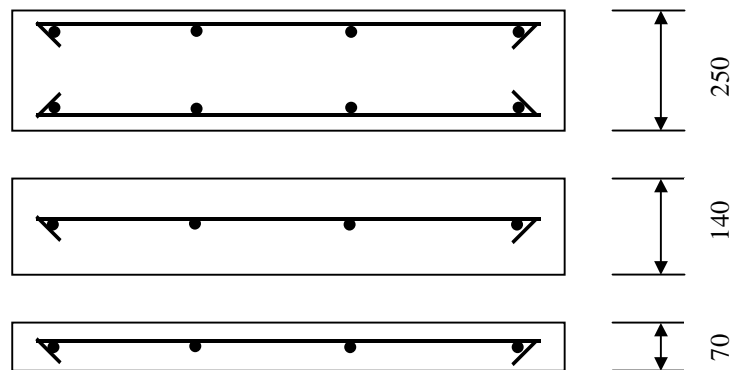

Figure 18: Reinforcement arrangement in the test samples.

The fragments were simulated by balls from a ballbearing with a diameter of 20,6 mm and a weight of 35,9 g. These balls, according to Erkander (1985), got a penetration equal to a fragment of two or three times the weight of the balls.

In total were 20 tests compared with numerical analysis whose results are summarized in Table 1 to Table 4. In the experiments the ingoing crater size (D_e), outgoing crater size (D_s), ingoing penetration (p_e), and the outgoing penetration (p_s) were measured, as visualized.
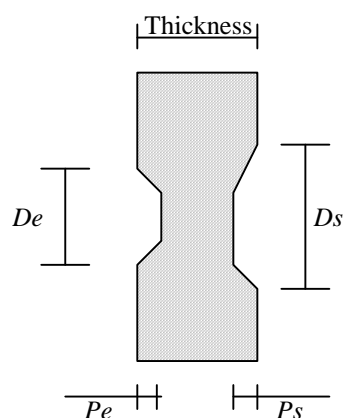

Figure 19: Notations for experimental results. Ingoing crater size ($\underline{D_e}$), outgoing crater size (D_s), ingoing penetration (p_e), and the outgoing penetration (p_s)

Table 1: Summary of test series 1.

Analysis reference	Quality of concrete	Thickness [mm]	Velocity [m/sec]	De [mm]	Pe [mm]	Ds [mm]	Ps [mm]
P60100	60	140	1024	270	50	380	46
P60200	60	140	1132	250	60	300	67
P60300	60	140	1163	240	66	310	65
P60400	60	140	1239	265	65	330	65
P60500	60	140	1283	230	50	360	80

Table 2: Summary of test series 2.

Analysis reference	Quality of concrete	Thickness [mm]	Velocity [m/sec]	De [mm]	Pe [mm]	Ds [mm]	Ps [mm]
P60600	25	140	1073	260	42	240	50
P60700	25	140	1060	220	43	270	50
P60800	25	140	982	190	55	280	47
P60900	25	140	925	190	48	300	50
P61000	25	140	859	190	42	200	0
P61100	25	140	1214	230	40	290	50

Table 3: Summary of test series 3.

Analysis reference	Quality of concrete	Thickness [mm]	Velocity [m/sec]	*De* [mm]	*Pe* [mm]	*Ds* [mm]	*Ps* [mm]
P63500	25	70	609	120	28	170	36
P63600	25	70	491	125	25	190	32
P63700	25	70	350	60	17	100	0
P63800	25	70	358	85	14	120	0
P63900	25	70	380	100	20	170	28

Table 4: Summary of test series 4.

Analysis reference	Quality of concrete	Thickness [mm]	Velocity [m/sec]	*De* [mm]	*Pe* [mm]	*Ds* [mm]	*Ps* [mm]
P66500	60	250	1201	240	67	0	0
P66600	60	250	1218	260	69	0	0
P66700	25	250	1204	270	52	0	0
P66800	25	250	1269	260	54	0	0

4.2 Analysis.

The analyses were carried out in Autodyn, using the RHT model for describing the concrete and a von Mises strength model describing the steel as mentioned in chapter 3. To minimize the computational calculations, the analyses were done in 2D and modelled with symmetry around the central axis as seen in Figure 20. The processor was as mentioned before the Lagrange processor which operates on a structured (I-J) numerical mesh. As seen in Figure 20 the element sizes for the two subgrids, one for the ball and one for the concrete wall, is very small but is chosen according to Zukas and Scheffler (2000), who made a study on the effect of meshing, which conclude that for accuracy there should be at least three elements across the radius of the projectile.
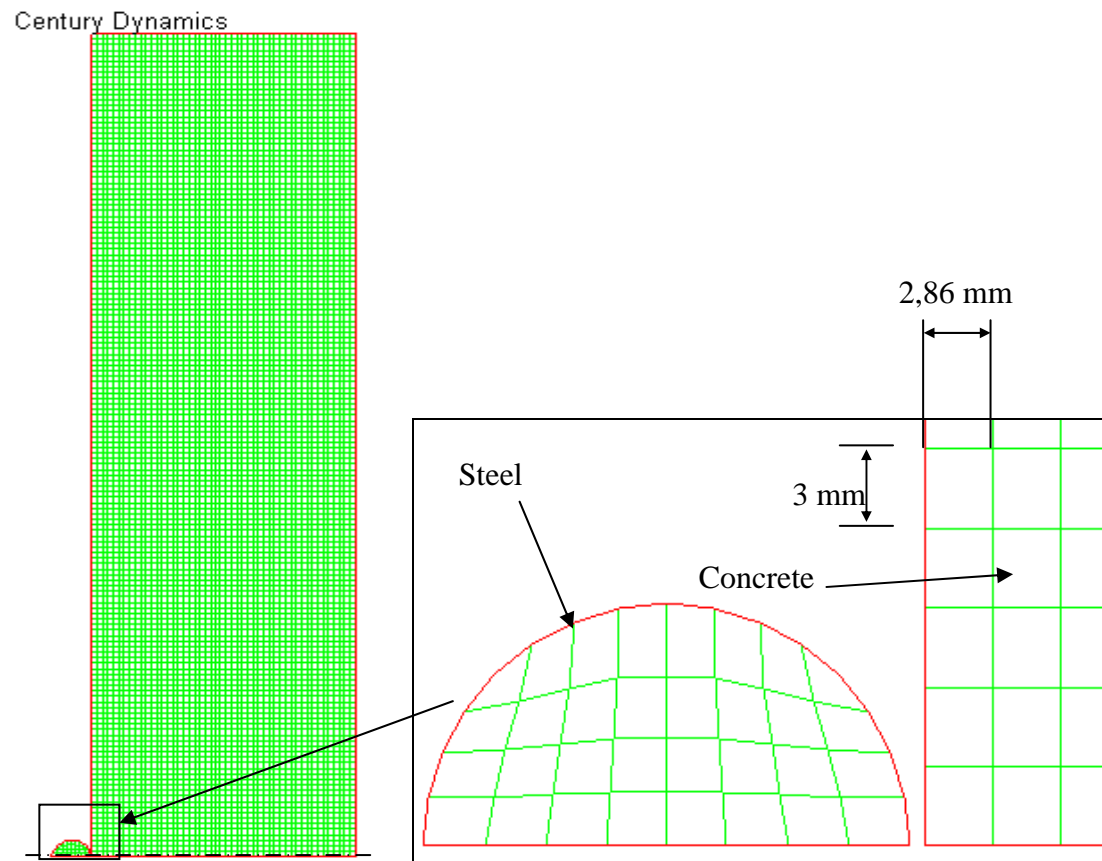

Figure 20: Mesh of subgrids.

The material model had to be calibrated for the two concrete materials according to their compressive strength i.e. their yield surface and the residual strength. As these are approximated with functions in Autodyn, equation 4.1 respectively 4.2 an initial calibration of the parameters involved had to be done.

$$fcm, cyl \left[A \left(p^* - p_{spall}^* \right)^N \right] \qquad \text{Yield surface} \qquad (4.1)$$

$$fcm, cyl \ B \left(p^* \right)^M \qquad \text{Residual strength} \qquad\qquad (4.2)$$

The compressive strength (cylinder standard) was calculated from at least 10 cubic tests of the concrete quality and converted to cubic standard according to Engström (1994). The strength-strain relationship and the residual strength were calculated for different lateral pressures according to the Attard model (1996). The Attard model was chosen because of its applicability to a wide range of concrete strengths and confinement pressures. When the strengths for different confinements were calculated it was to calibrate equation (4.1) and (4.2) to fit the curve given from the Attard model. In Figure 21 it is seen that the residual curve from Attard cross the yield strength at 53 MPa hydrostatic pressure, which is not correct. The residual strength can never be more than the yield strength. The model, though, calculates according to the function called residual_model in Figure 21, which is a good approximation of the residual strength.
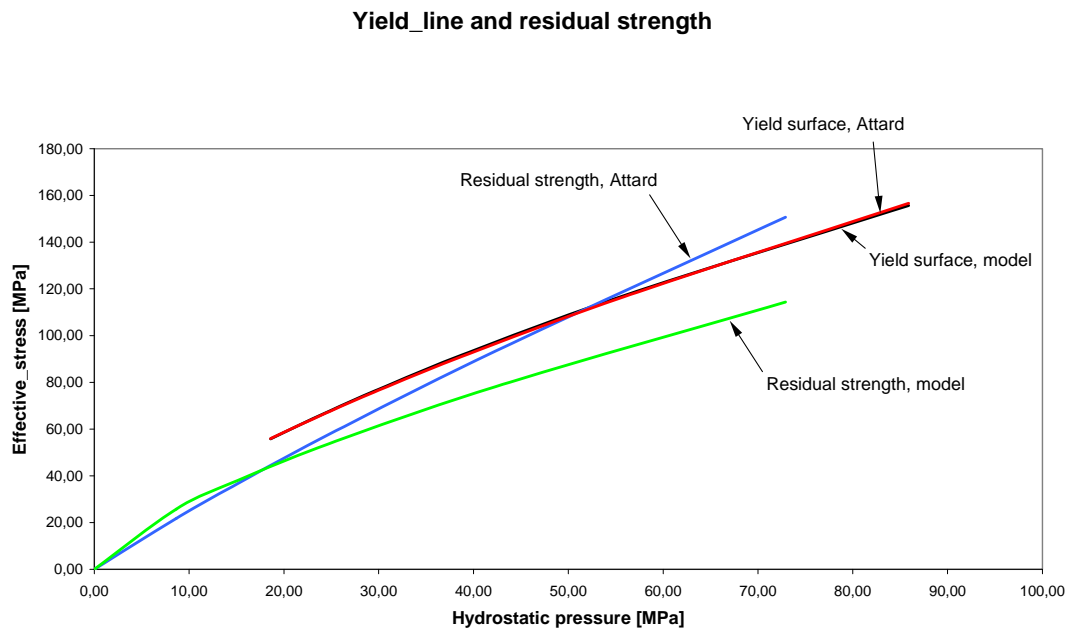
Yield_line and residual strength

Figure 21: Yield line and residual strength.

From CEB-FIB model code (1990) the fracture energies was taken according to tabulated values and the tensile strength was calculated from equation (4.3).

$$fctm = fctk0, m \left(\frac{fck}{fck0} \right)^{2/3} \qquad\qquad (4.3)$$

where:

$fctk0.m = 1,40 \ \text{MPa}$

$fck0 \ = 10 \ \text{MPa}$

The elasticity modulus was also calculated according to model code with equation (4.4).

$$Eci = E_{c0}\left[\frac{fcm}{fcm0}\right]^{1/3}$$

(4.4)

where:

$$E_{c0} = 2{,}15 \times 10^4 \text{ MPa}$$
$$fcmo = 10 \text{ MPa}$$

The shear modulus was calculated according to equation (4.5).

$$G = \frac{E}{2(1+\upsilon)} \qquad \upsilon = 0{,}3 \text{ for concrete}$$

(4.5)

4.3 Parameter study.

A parameter study was carried out to be able to evaluate the influence that the different parameters have on the dynamic tensile strength, crater sizes, and penetration depth. The parameters looked upon are the *Frate*, further explained below, static shear strength, static tensile strength, and the fracture energies of the modelled material. The result of the parameter study was then used as a base for finding an adequate model of concrete. The study was carried out in the same way and with the same definitions as the analysis. From a reference analysis, the parameter was changed and the result was evaluated. As seen in Figure 22, the stress-strain relationship in direction 2 is measured on the opposite side of the fragment entrance and the penetration is measured from the initial position of the entrance border to the ball midpoint. The crater sizes are evaluated from the reference analysis and the effect of the parameter, in percentage, is shown in plots of the material status.
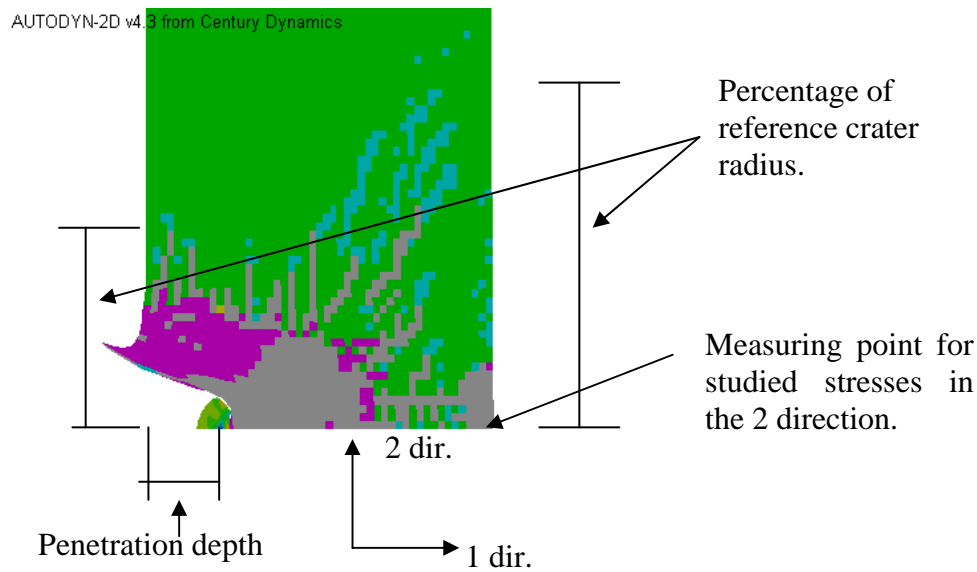
Figure 22: Guidance to studied results.

A summarize of the importance that each parameter has is made in Table 5, shown by large or small influence on the tensile resistance, outgoing and ingoing crater size, and the penetration.

Table 5: Influence of parameters included in the parameter study.

Parameter	Influence on the tensile resistance	Influence on the outgoing crater size.	Influence on the ingoing crater size.	Influence on the penetration.
Frate	Large	Small	Small	Small
Shear resistance	Large	Large	Large	None
Tensile resistance	Large	Large	Large	None
Softening Energies	-	-	-	-

4.3.1 Strain Rate

The *Frate* parameter considers the strain rates and influences directly the failure surface by the δ factor in the formula defining the *Frate*, seen in equation (2.10). The *Frate* is a scaling factor and the effect of increased δ is seen in equation (4.6), a higher *Frate* need a higher tensile stress to reach failure, which is verified by the results in Figure 23, i.e. higher δ gives a higher tensile capacity. And the conclusion could be

drawn that the tensile strength is highly influenced by the strain rate. δ is notated D in the rest of the report

$$f\left(P, \sigma_{eq}, \theta, \dot{\varepsilon}\right) = \sigma_{eq} - Y_{TXC(P)} * F_{CAP(P)} * R_{3(\theta)} * F_{RATE(\dot{\varepsilon})} \qquad (4.6)$$

$$f\left(P, \sigma_{eq}, \theta, \dot{\varepsilon}\right) = 0 \;\rightarrow\; \text{Failure is reached.} \qquad (4.7)$$
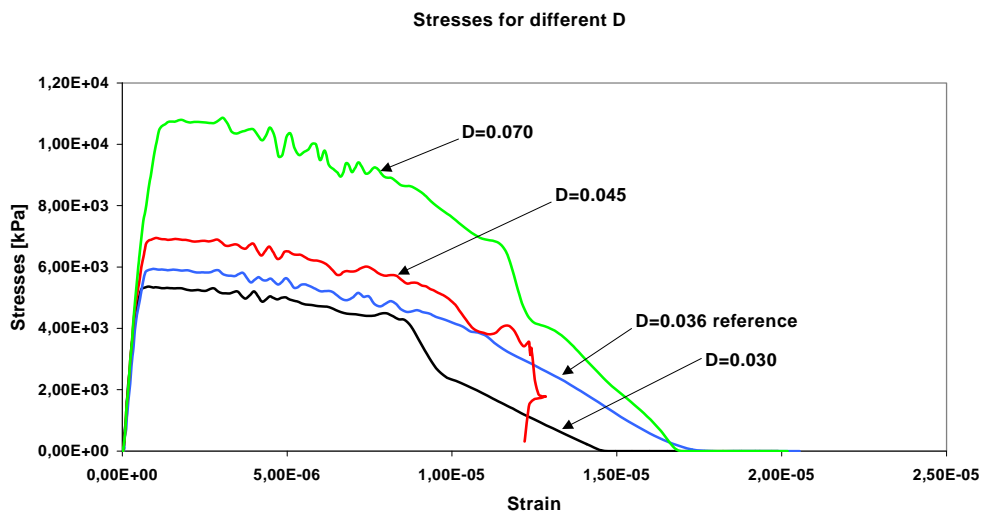

Figure 23: Stress Strain direction 2 in target point 7 for different D
(0.030,0.036,0.045,0.07).

The effect on the crater sizes are, however, small as seen in the material status plots, Figure 24, Figure 25, Figure 26. The small changes seen are explained by the reason that a lower δ gives bigger crater on both sizes but the effect is still small. The changes in crater size derive from the lower respective higher tensile strength, which is further concluded to be related to the strain rate.
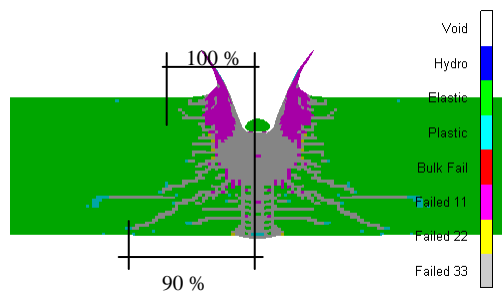

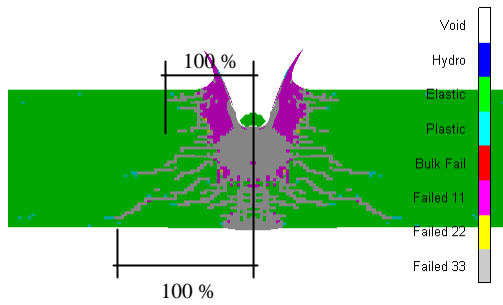*Figure 24: Material Status plot for D = 0.045.*

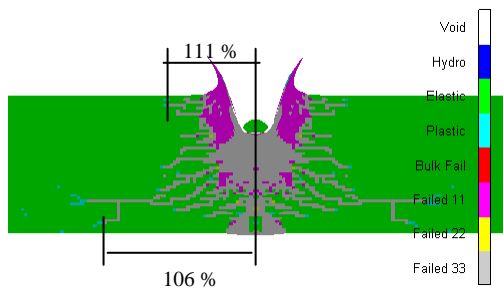*Figure 25: Material Status plot for D = 0.036 (reference).*

Figure 26: Material Status plot for D = 0.030.

The penetration becomes smaller for larger *D*, seen in Figure 27, but the effect is rather small. That small that it could be neglected; a 16 % decrease of *D* gives only a 3 % increase of the penetration. The change could though be explained by the lower tensile strength coming from the lower strain rate that a decrease of *D* gives.
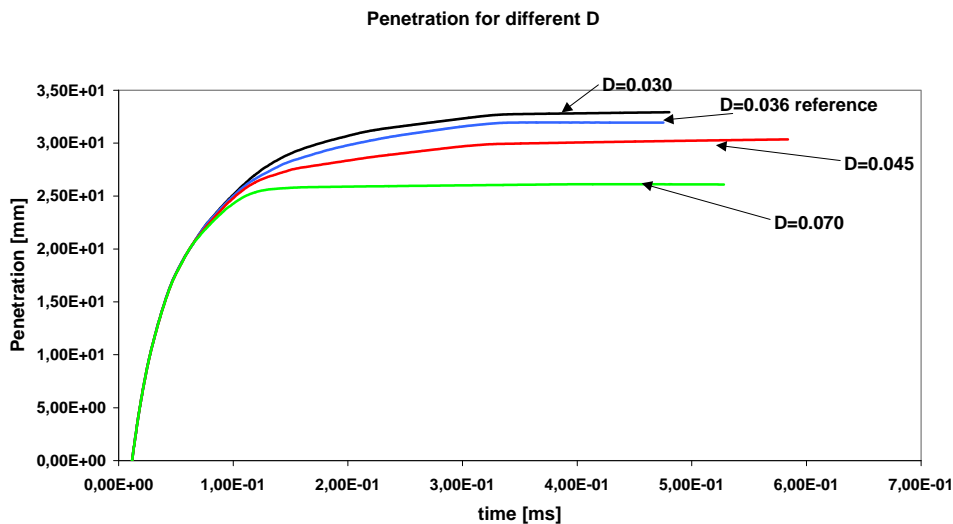

Figure 27: Penetration for different D.

When studying the strain rates effect on the specimen, it is also convenient to see at which point or how the strain rates are distributed over the section. As seen in Figure 28, in the penetration area, i.e. in front of the fragment, in which the material is

under severe loading and completely compressed the strain rates are very high. However, outside the penetration area it is possible to se the development of the cracks according to the strain rates. The different points studied are evaluated with its highest and lowest strain rates during the whole simulation, positive value for compression and negative value for tension. The true craters are also visualized. It is seen that the strain rates decrease with a factor of 10, for every point row studied moving upward in the figure from the symmetrical border. It is also seen that where the largest negative strain rates occur is where the largest crack patterns develop, which could explain the larger crater size on the backside of the specimen i.e. larger strain rates in tension further away from the symmetrical border on the backside of the specimen.
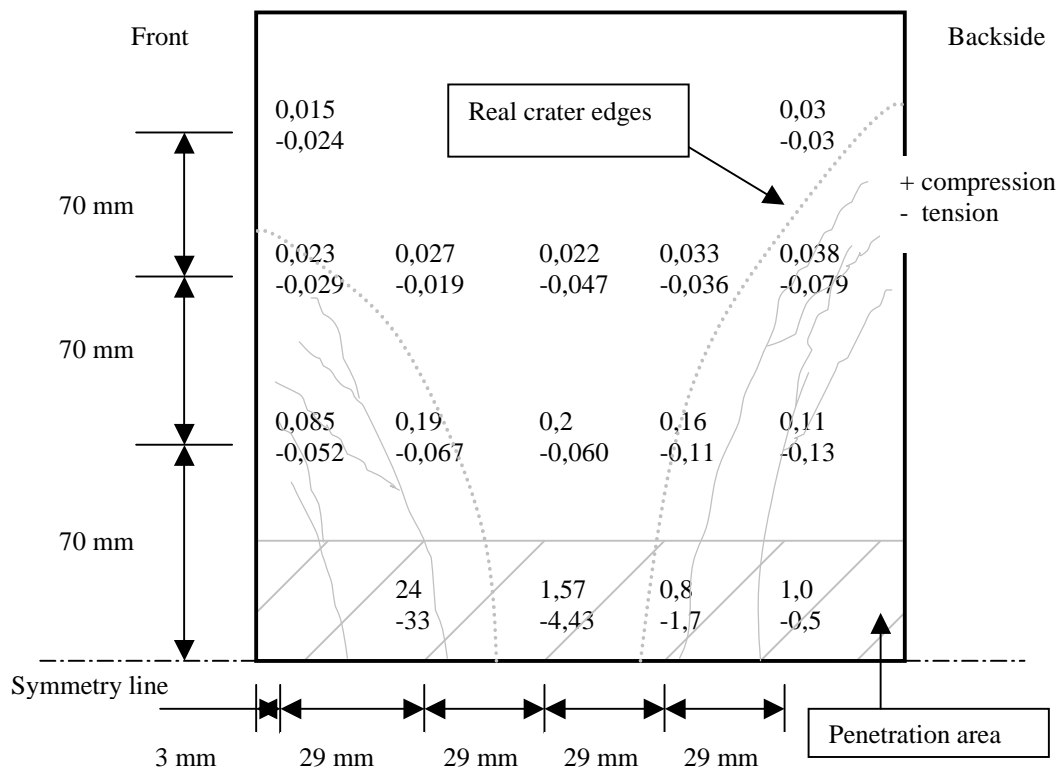
Figure 28: Maximum and minimum strain rates at different locations in the section during penetration.

The differences in longitudinal and transversal strain rates in Figure 28 are explained by the difference in velocity of a wave travelling in longitudinal respectively transversal direction. According to Leppänen (2001) is the difference approximately 60 %, i.e. the strain rate in transversal direction is 60 % of the strain rate in longitudinal direction, measured at the same time.

4.3.2 Shear force.

The shear force resistance is set as a scaling parameter of the compressive strength in Autodyn. The default value is set to 18 % which could seem to be a bit high. While

studying the effect that the static shear resistance has on the dynamic tensile resistance, i.e. the higher strength given at higher strain rates, it is seen that a greater shear resistance result in a smaller dynamic tensile resistance, visualized in Figure 29. The effect could be related to a scaling of the RHT concrete failure surface but the explanation of this is left for future studies. But still the parameter is used for calibrating the material model.
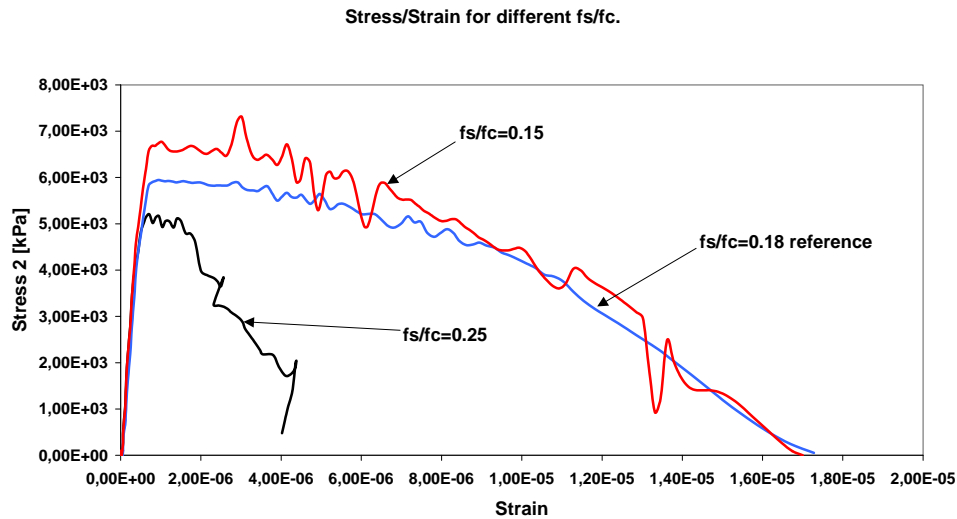
Figure 29: Stress/strain for different fs/fc.

In Figure 32 to Figure 30 it is seen that the crater size on the outgoing side is highly more affected by changes of the shear resistance. A decrease with 3 % gives a change of 65 % on the outgoing crater size, which is a result of the great difference in dynamic tensile strength between small changes in the static shear resistance.
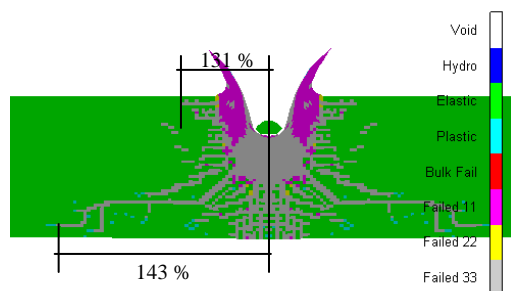
Figure 30: Material status plot for fs/fc = 0.25.
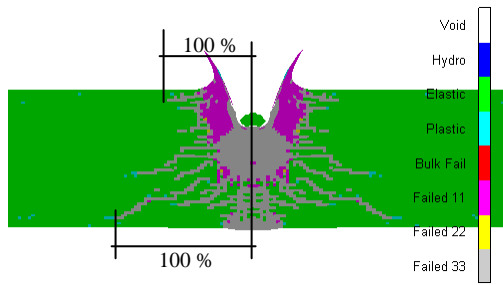
Figure 31: Material status plot for fs/fc = 0.18 (reference).
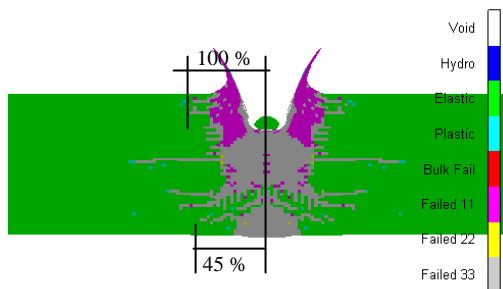
Figure 32: Material status plot for fs/fc = 0.15.

In the penetration depth it is not possible to see any effect of the change in shear resistance, see Figure 33.
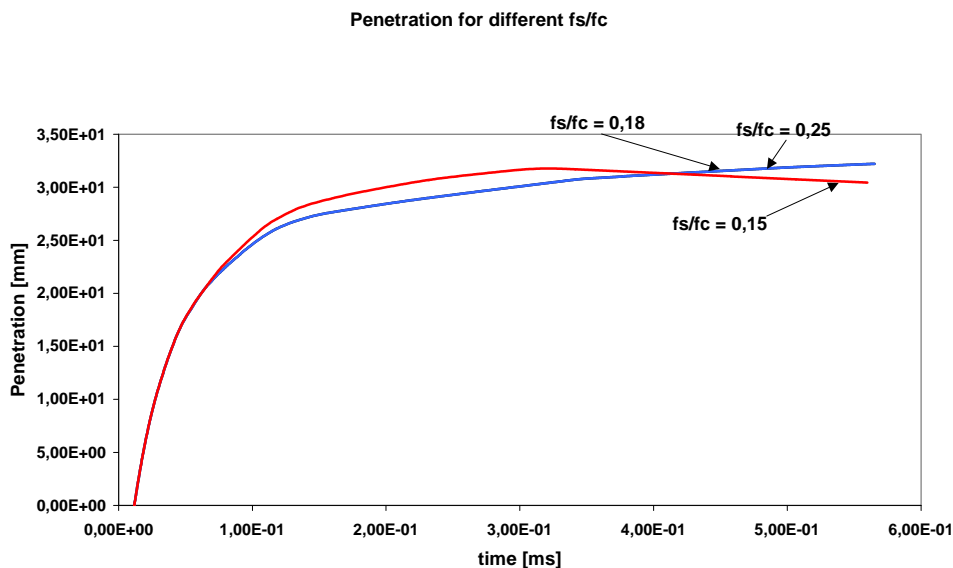
Figure 33: Penetration for different fs/fc.

4.3.3 Tensile force

It would be strange if a higher tensile strength did not affect the tensile failure stress in the model. To prove the obvious Figure 34 show the tensile failure stress for

changes of the static tensile resistance. The quick descend for *ft/fc* = 0.08 shows the failure of the picked element.
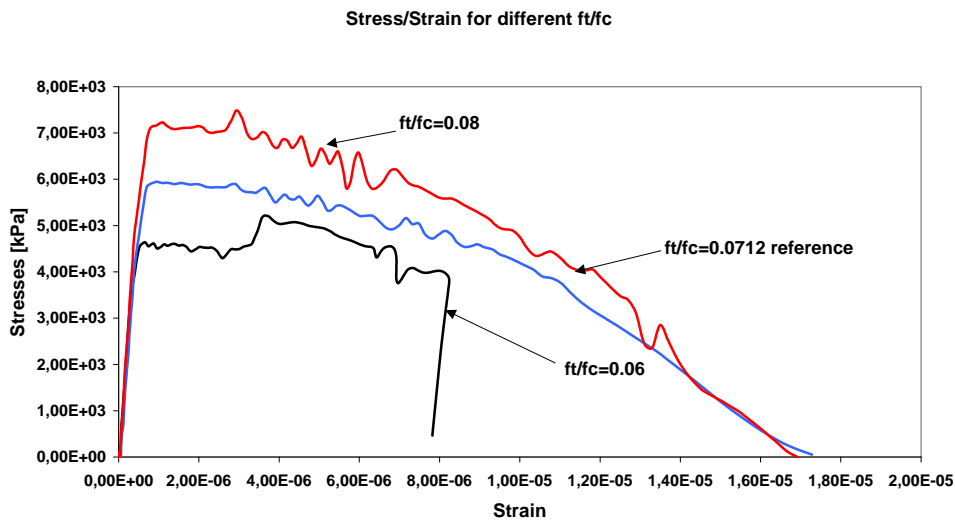
Figure 34: Stress Strain direction 2 in target point 7 for different ft/fc.

The effect of changes in the static tensile strength on the crater size seem to be reasonable as a decrease of 1 % gives a approximated decrease of the crater size of 10 %, seen in Figure 35, Figure 36, and Figure 37.
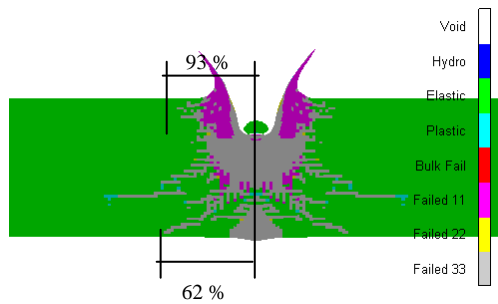
Figure 35: Material Status plot for ft/fc=0.080.
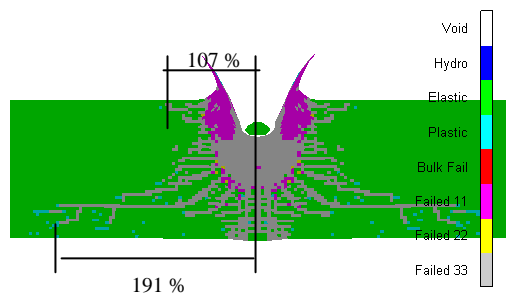
Figure 36: Material Status plot ft/fc=0.060.
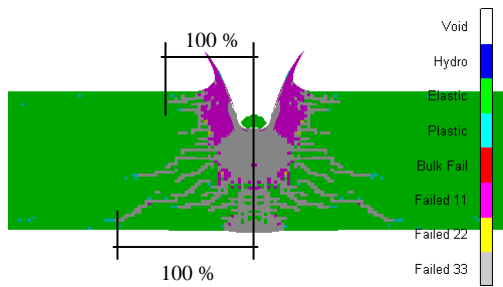
Figure 37: Material Status plot ft/fc=0.0712 (reference).

Something that is less obvious is that changes in the static tensile resistance only give small, close to zero, effect on the penetration of the fragment, seen in Figure 38. It is concluded then, that the penetration depends more or less only on the compactation of the material and so forth is the penetration related to the static compressive strength.
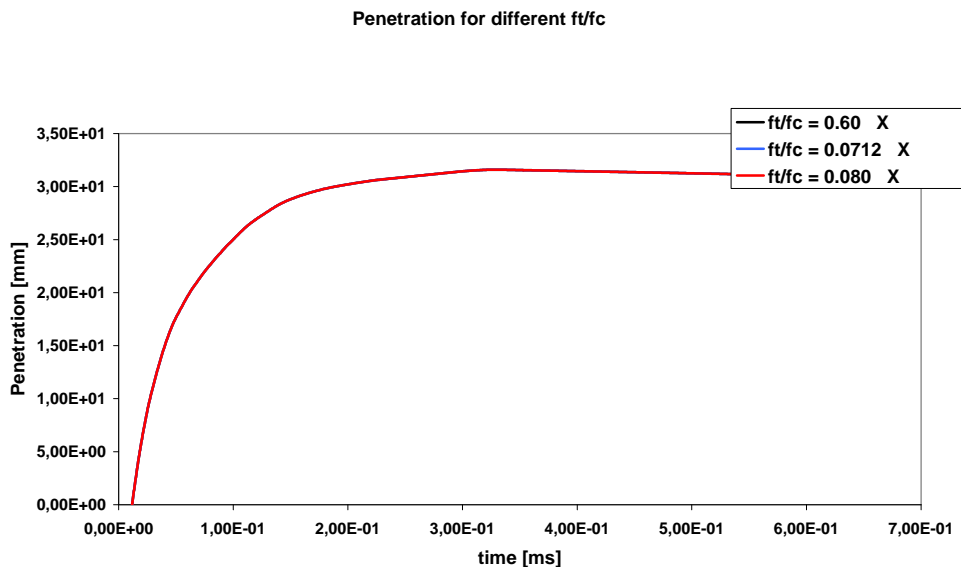
Figure 38: Penetration for different ft/fc[1]

4.3.4 Crack softening.

Changes in the crack softening parameter *Gf* (J/m^2) within 50 % give no excessive changes in the response as seen in

Figure 40 to Figure 43, showing the same material model with different crack energies. This seems strange, as a halving of the softening energies should result in a halving of the area of the descending branch in the stress strain relationship shown in Figure 39. This behaviour appears to be due to a limitation in the software. The

---

[1] Plots for *ft/fc*=0.060, *ft/fc*=0.0712 and *ft/fc*=0.080 is exactly the same and are thereby shown on top of each other.

software demands that an ultimate tensile strength is set so it can consider the crack energies in the calculation. This act, however, results in that the higher dynamic tensile strength gained by the high strain rate, threatened in Chapter 2.2, is not reached, seen in the graph P6FT39 in Figure 39, where the ultimate tensile strength is set to 3,973 MPa according to the static tensile resistance. Because of these problems with the software the crack energies are not furthermore involved in the parameter study.
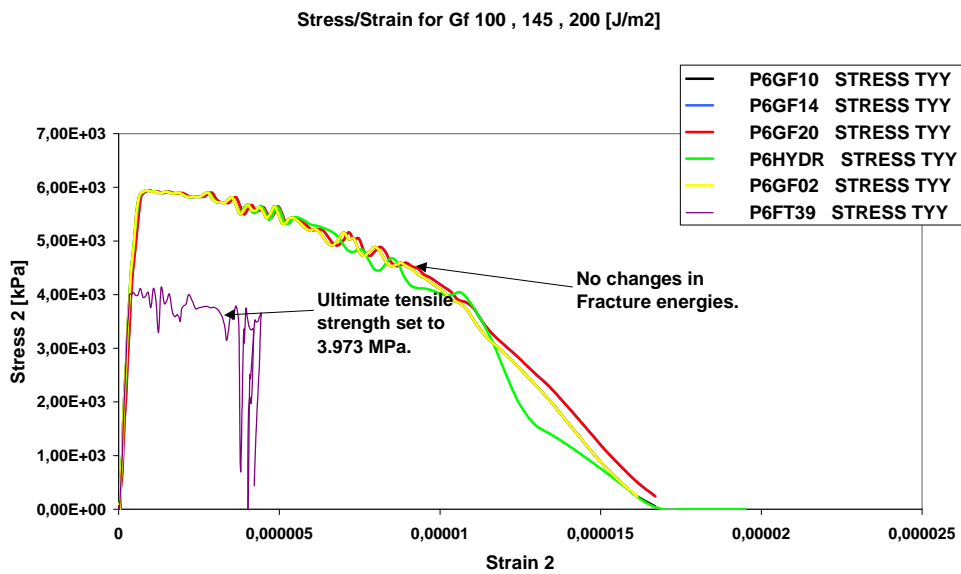
Figure 39: Stress Strain direction 2 in target point 7 for different Gf
(100,145,200[J/m2]).

The material plots are all the same as there is no change in the response.
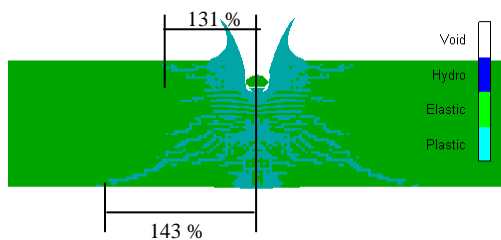
Figure 40: Material status plot for hydro failure model.

Figure 41: Material status plot Gf = 200 [J/m2]
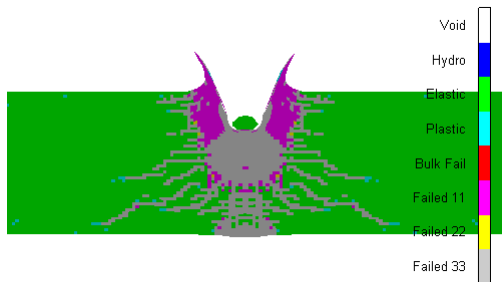
Figure 42:Material status plot Gf = 145 [J/m2]
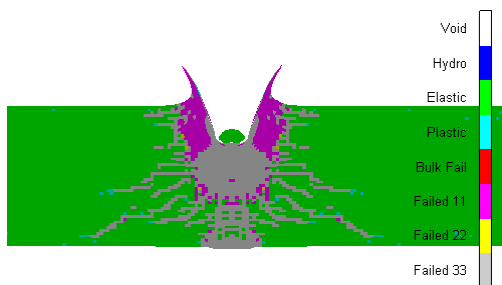
Figure 43:Material status plot Gf = 100 [J/m2]

It is also seen in Figure 44 that the penetration of the fragment neither is affected by changes of the crack energies.
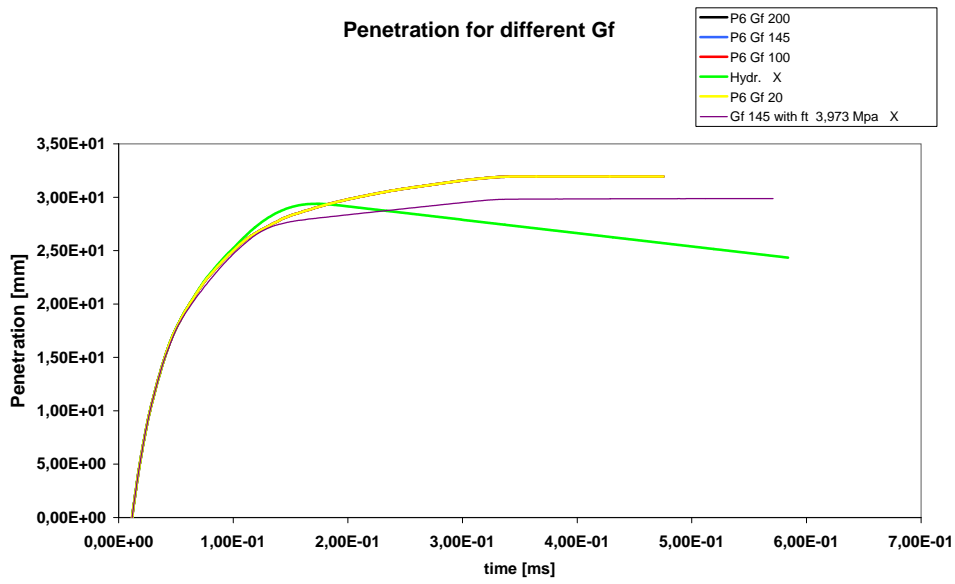
Figure 44: Penetration for different Gf (20,100, 145, 200 [J/m2])[2] .

---

[2] Plots for *Gf*=100 J/m^{2}, *Gf*=145 J/m2 and *Gf*=200 J/m2 is exactly the same and are thereby shown on top of each other.

4.3.5 Results from parameter study.
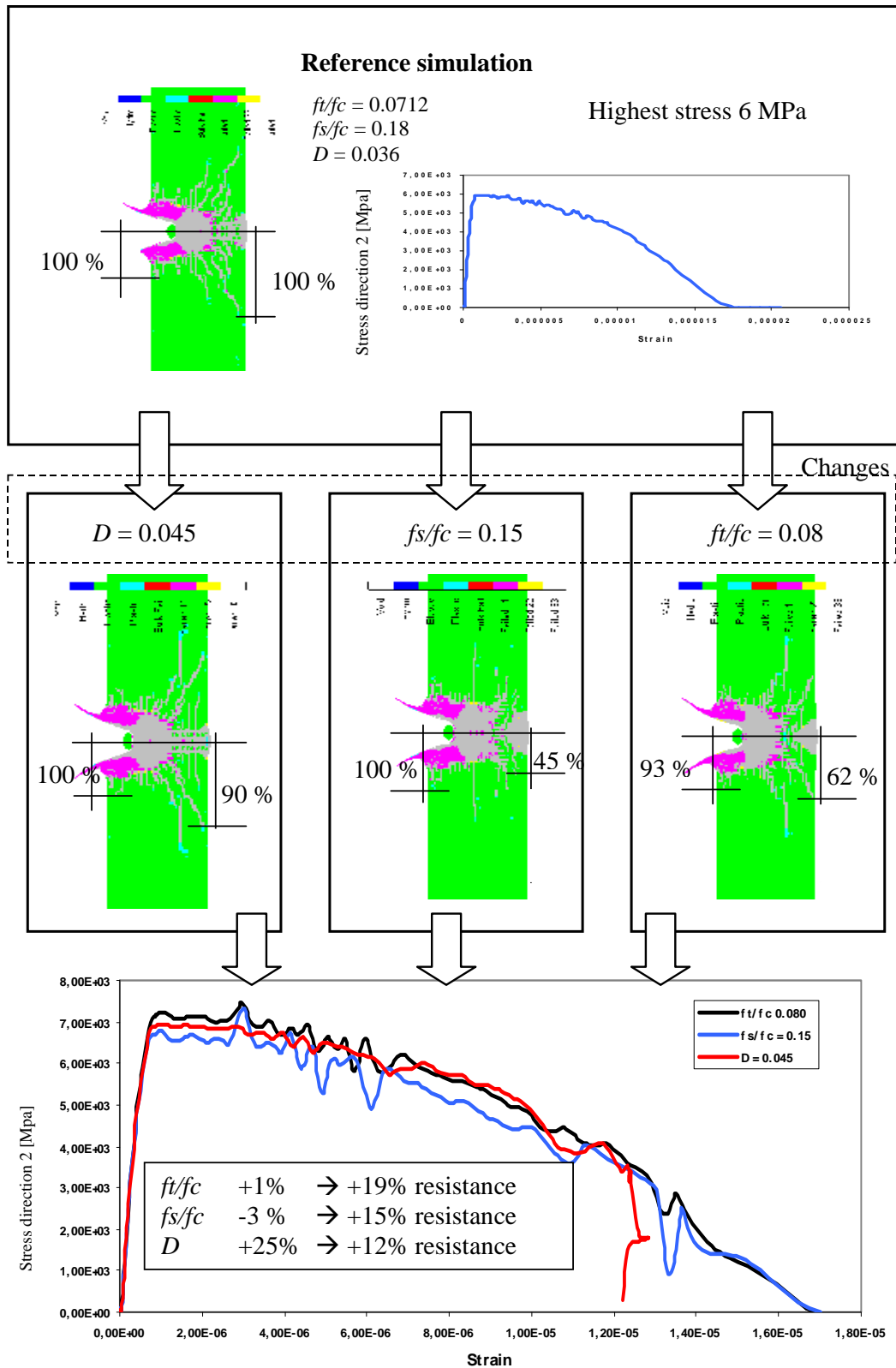
Figure 45: Summary of changes that give an increase in dynamic resistance.
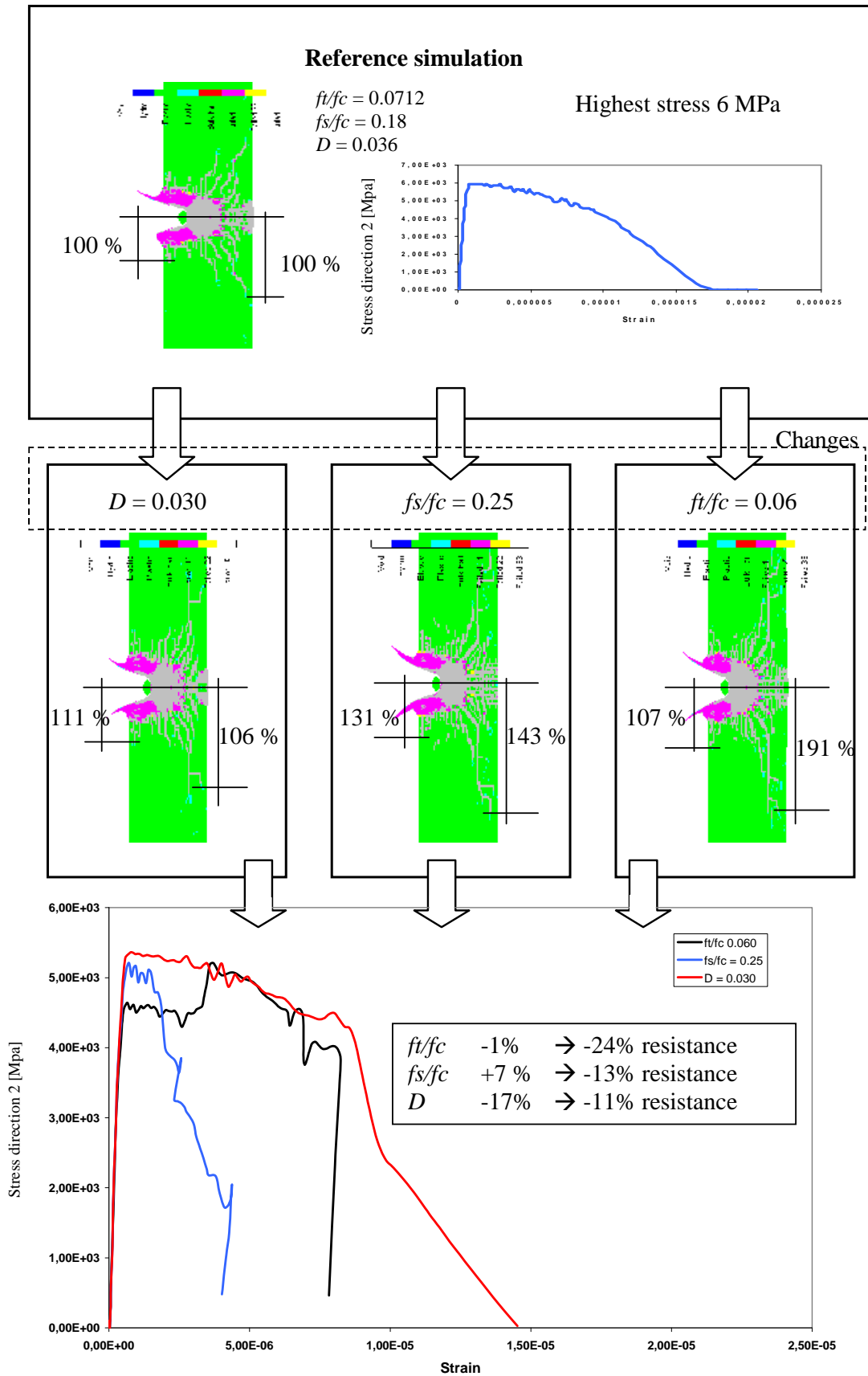
Figure 46: Summary of changes that give a decrease in dynamic resistance.

4.4 Calibration of parameters.

The calibration process was supposed to be based on the results from the parameter study but became a process more based on the results from the full-scale tests. The knowledge gained from the parameter study was only valuable for knowing in which direction to go, if the value of the parameter would be increased or decreased. The calibration started at a rather wide range of values which was narrowed down towards a final value. Finally, the value of the quote *fs/fc* was set to 0.17 but the *D* parameter, conducting the strain rate, still gave good results for C60 at 0.033 and for C25 at 0.032. Why a calibration in-between these values were performed to make a compromise between the two concrete classes and in the end the parameter *D* was set to 0.0328. Examples of the calibration analyses are added in the appendix, showing the crack pattern and the real crater size for that certain analysis. During the process the analyses were awarded with stars according to their accuracy with the result from the belonging full-scale test. One star was given for good results i.e. the results from the analyse fit rather good to the experimental results. Two stars were given to very good results; and for those without stars, the results were not promising. The process is visualized in Figure 47.

Analysis	D	fs/fc	Stars
P60500	0.035	0.18	
P60501	0.035	0.17	
P60502	0.035	0.16	
P60503	0.034	0.18	
P60504	0.034	0.17	
P60505	0.034	0.16	
P60506	0.033	0.18	
P60507	0.033	0.17	☆
P60508	0.033	0.16	
P60509	0.032	0.18	☆ ☆
P60510	0.032	0.17	☆ ☆
P60511	0.032	0.16	

Analysis	D	fs/fc	Stars
P60602	0.034	0.17	☆
P60603	0.034	0.16	
P60604	0.034	0.15	
P60605	0.034	0.14	
P60606	0.033	0.17	☆ ☆
P60607	0.033	0.16	
P60608	0.033	0.15	
P60609	0.032	0.17	
P60610	0.032	0.16	
P60611	0.032	0.15	

Analysis	D	fs/fc	Stars
P60612	0.033	0.175	☆ ☆
P0613	0.0325	0.175	
P60513	0.0325	0.175	☆ ☆
P60512	0.032	0.175	

| Analysis	D	fs/fc	Stars
P60617	0.0326	0.17	☆
P60616	0.0327	0.17	☆
P60615	0.0328	0.17	☆ ☆
P60614	0.0329	0.17	☆
P60517	0.0326	0.17	☆
P60516	0.0327	0.17	☆
P60515	0.0328	0.17	☆ ☆
P60514	0.0329	0.17	☆

Analysis	D	fs/fc	Stars
P66500	0.035	0.18	
P66501	0.035	0.17	
P66502	0.035	0.16	
P66503	0.034	0.18	
P66504	0.034	0.17	
P66505	0.034	0.16	
P66604	0.033	0.18	
P66607	0.033	0.17	
P66608	0.033	0.16	

D = 0.0328

fs/fc = 0.17

Figure 47: Calibration process.

4.5 Parameters in RHT model.

The parameters used, for the two concrete types C60 and C25, in the RHT model are presented in Table 1. The values are obtained from the experience gained in the parameter study presented in chapter 4.3 and while trying to get the same results in the analyses as in the full scale tests presented in chapter 4.1.

Table 6: Parameters in RHT concrete model.

STRENGTH MODEL: RHT Concrete	C60	C25
Shear Modulus (kPa)	1.47000E+07	1.47000E+07
Compressive Strength *fc* (kPa)	5.58000E+04	2.967000E+04
Tensile Strength *ft/fc*	7.12000E-02	7.887000E-02
Shear Strength *fs/fc*	1.70000E-01	1.70000E-01
Failure Surface Parameter *A*	2.05000E+00	2.05000E+00
Failure Surface Exponent *N*	7.00000E-01	8.00000E-01
Tens./Compr. Meridian Ration	6.80500E-01	6.80500E-01
Brittle to Ductile Transit.	1.05000E-02	1.05000E-02
G(elas.)/G(elas.-plas.)	2.00000E+00	2.00000E+00
Elastic Strength/*ft*	7.00000E-01	7.00000E-01
Elastic Strength/*fc*	5.30000E-01	5.30000E-01
Use Cap on Elastic Surface	1.00000E+00	1.00000E+00
Residual Strength Const. *B*	1.70000E+00	2.50000E+00
Residual Strength Exponent *M*	7.00000E-01	7.00000E-01
Comp. Strain Rate Exponent *a*	3.20000E-02	3.20000E-02
Tens. Strain Rate Exponent *D*	3.28000E-02	3.28000E-02
Max. Fracture Strength Ratio	1.0000E+20	1.0000E+20
FAILURE MODEL: RHT Concrete		
Damage Constant *D1*	4.00000E-02	4.00000E-02
Damage Exponent *D2*	1.00000E+00	1.00000E+00

Min. Strain to Failure	1.00000E-02	1.00000E-02
Residual Shear Modulus Frac.	1.30000E-01	1.30000E-01
Tensile Failure Model	Principal Stress	Principal Stress
Tensile Failure Stress (kPa)	1.01000E+20	1.01000E+20
Maximum Shear Stress (kPa)	1.01000E+20	1.01000E+20
Crack Softening, Gf (J/m2)	1.45000E+02	1.45000E+02
or, $Kc2$ (mN2/mm3):	5.61449E+09	5.61449E+09
EROSION MODEL: Instant Geometric Strain		
Erosion Strain	2.00000E+00	2.00000E+00

4.6 Results.

The model after calibration, i.e. the parameters are set according to table 6, was verified to results from full-scale tests. In general, it could be stated that it works satisfactorily describing the crack pattern on the backside of the member, the so-called outgoing crater. However, on the front side the result is not that convincing, the model gives a crack pattern of the ingoing crater that tends to develop according to the related full-scale experiments but it does not reach full satisfactory status, except for thinner walls. This could be the cause of that the crack energy have not been implemented, something that could give better results even on thicker walls. Regarding the velocity it is not seen that any velocity, high or low, give good results or not and it could therefore be concluded that the model works properly for all velocities, ranging from 600 m/s to 1000 m/s.

In this chapter are the results from the verification presented with the real crater sizes visualized with dotted lines. There are walls presented for every thickness, 70 mm, 140 mm and 250 mm, and concrete classes, C25 and C60, concerned in the study.

Figure 48 to Figure 51 shows the result for the walls with the thickness 140 mm. It is seen that the model give good result on the backside but bad results on the front side. Result for the walls with the thickness 70 mm are shown in Figure 52 and Figure 53. It is seen that for this thickness the result on the ingoing side also is convincing. Figure 54 shows an example of the result on a 250 mm thick wall. It can be seen that the result is not good as the fragment only penetrate and not perforate the wall. Thus, only give result on the ingoing side.

Real crater size.

p60100
Cycle 20000
Time 7.980E-001 ms
Units mm, mg, ms

D 3.28E-3 FS/FC 0.17 C 60
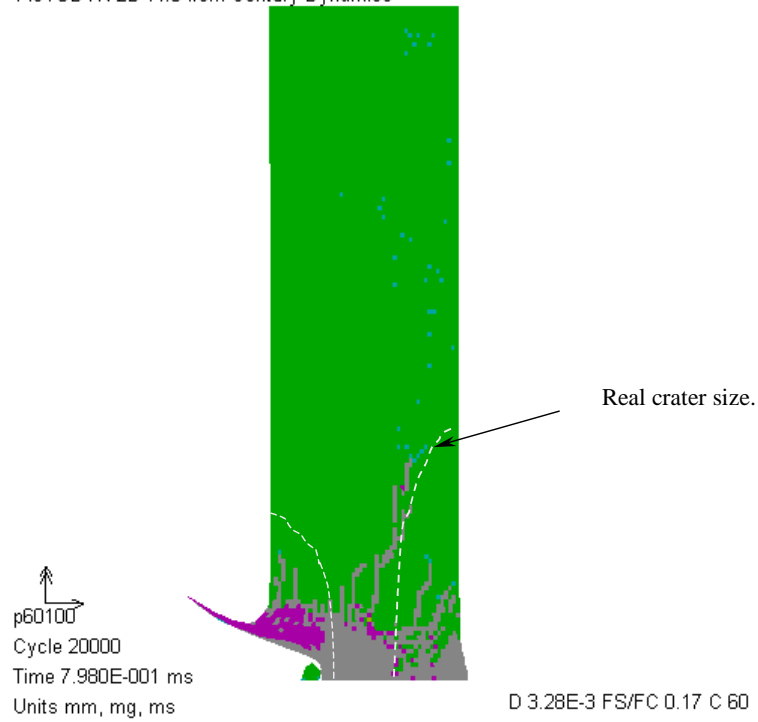
Figure 48: Analysis P60100, see table 1, with the real crater edge as dotted line.

p60200
Cycle 20000
Time 6.865E-001 ms
Units mm, mg, ms

D 3.28E-3 FS/FC 0.17 C 60
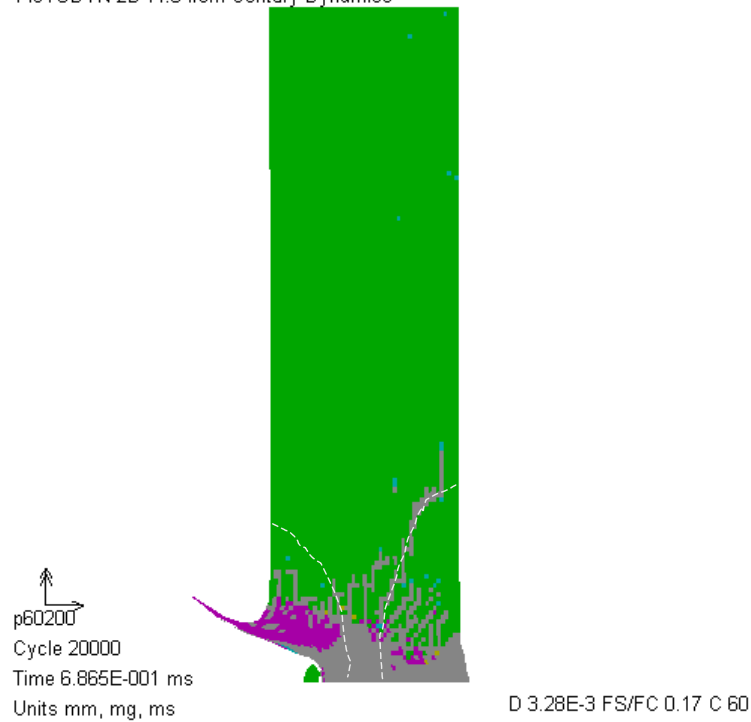
Figure 49: Analysis P60200, see table 1, with the real crater edge as dotted line.

AUTODYN-2D v4.3 from Century Dynamics

p60300
Cycle 20000
Time 7.535E-001 ms
Units mm, mg, ms

D 3.28E-3 FS/FC 0.17 C 60
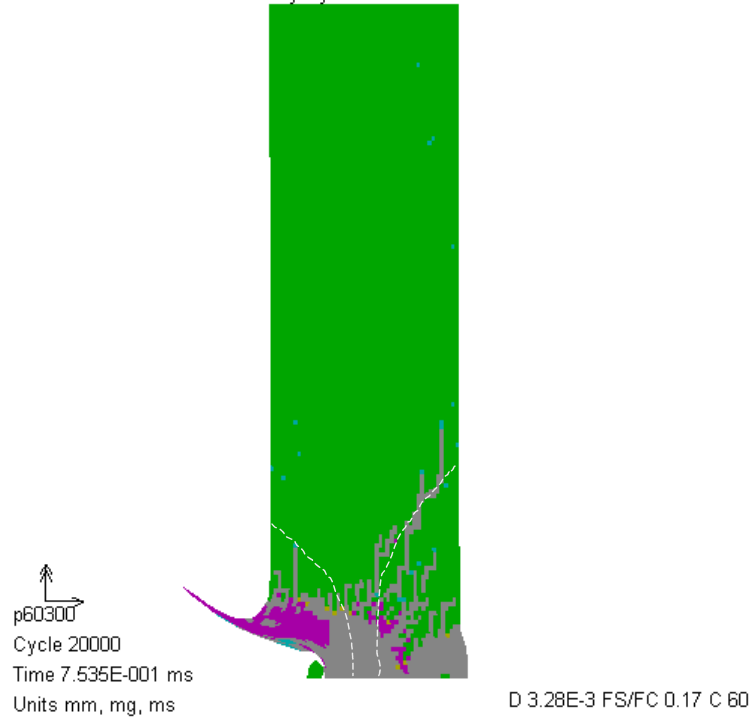
Figure 50: Analysis P60300, see table 1, with the real crater edge as dotted line.

AUTODYN-2D v4.3 from Century Dynamics

p60600
Cycle 20000
Time 7.655E-001 ms
Units mm, mg, ms

D 3.28E-2 FS/FC 0.17 C 25
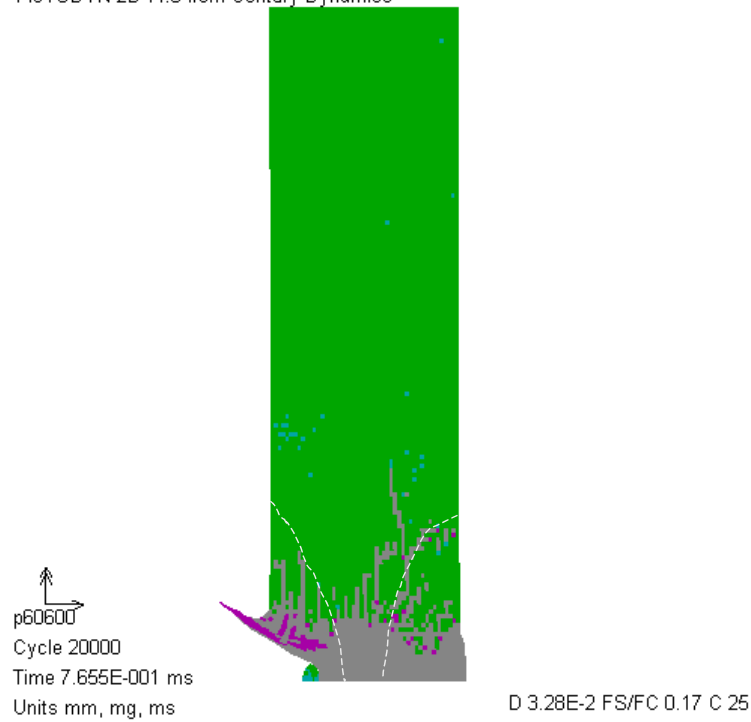
Figure 51: Analysis P60600, see table 1, with the real crater edge as dotted line.
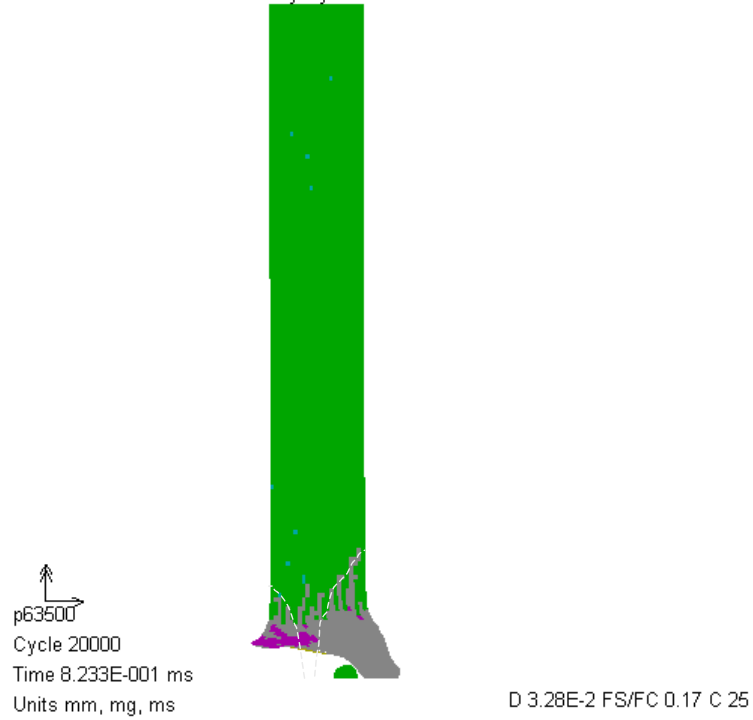
Figure 52: Analysis P63500, see table 1, with the real crater edge as dotted line.
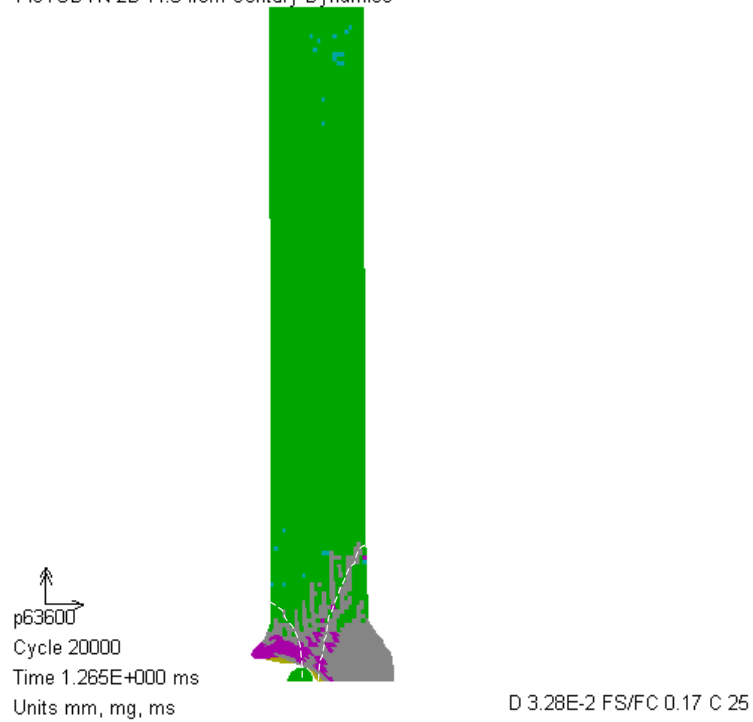
Figure 53: Analysis P63600, see table 1, with the real crater edge as dotted line.
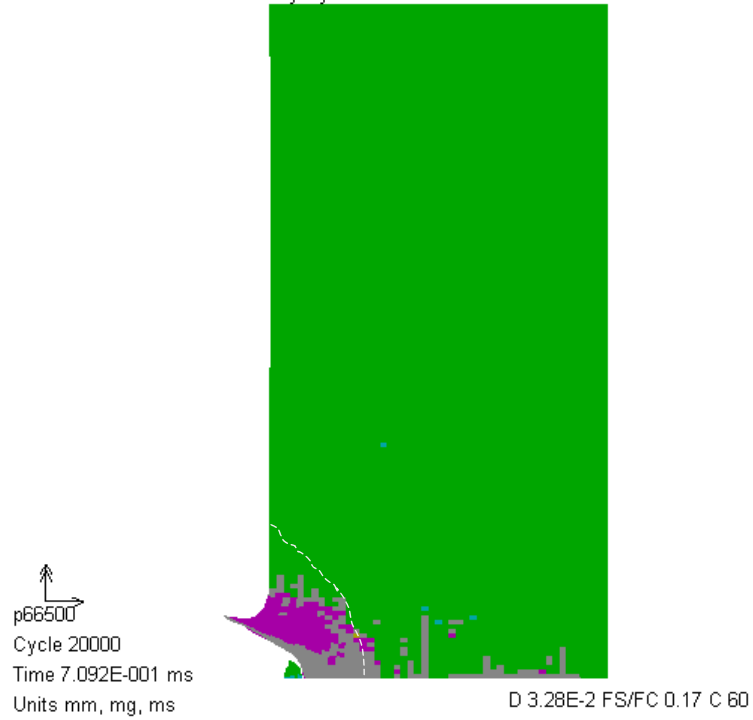
Figure 54: Analysis P66500, see table 1, with the real crater edge as dotted line.

5 Conclusions.

Civil defence shelters shall be designed to resist explosions caused by military weapons such as a conventional bomb. When fragments from such an explosion impact constructions, the fragments penetrate or even may perforate the construction wall causing damage in the total height of the wall. Almost all penetrations that is fairly deep cause scabbing on the backside of the construction wall generated by very high tensile stresses. The thesis aims to make it possible to simulate a fragment which perforates a concrete wall using numerical calculations in the software Autodyn. The high velocity of the fragment causes high strain rates, i.e. the velocity of the deformation in the deformed concrete. Autodyn considers the increase in strength with strain rate in its numerical analysis by a parameter named *Frate*. The *Frate* parameter is dependent on the actual strain rate, a reference strain rate, and a user definable parameter *D*.

When concrete is loaded under severe strain rates, the static resistance increases to a higher "dynamic" resistance. The increase in strength with strain rate is divided into two parts. The lower part, considering lower strain rates, depends on the water content and the higher strain rate is related to forces of inertia. The increase in strength for the strain rates related to water content is explained by the Stefan effect and by the internal pressure in the pore. For pores loaded parallel the Stefan effect says that the existence of a thin viscous film, like water, between two perfectly parallel plates separated by a distance, causes a counteracting force when the two plates are separated, which produces the increase in strength. For pores loaded perpendicular to the load, the increase in strength is explained by the alteration in pressure inside the pore, caused by the compressive force. The alteration in pressure counteracts the compression and the compressive strength increases.

When the fragment hits the concrete the deformation begins. A wave is initiated causing a triangular compressive stress over time, which travels faster in front of the fragment than in the perpendicular directions.

The wave producing the compressive stresses also causes the tensile stresses by the fact that when the wave reach the border of the wall the wave is reflected and goes back generating tensional stresses equal to the compressive stresses in magnitude. Since the tensile strength is much lower than the compressive strength for concrete the reflected wave could cause scabbing on the backside of the specimen.

There exist two main processors for numerical calculations by finite elements, one for modelling solid material and structures called Lagrange, and one for modelling fluid material and large distortions named Euler. The Euler processor uses a fixed mesh in which the material transforms. The mesh in the Lagrange processor follows the material as it deforms and the material stays inside the initial element definition with no transport of material between elements. The advantage of this, according to the Autodyn manual, tends to be that the computational process is fast. For this reason the Lagrange processor have been used as processor.

For a static numerical analysis the EOS, equation of state, normally describes the material behaviour when it is exposed to a load and is generally assumed to be linear. However, for severe loading it is essential to take into account the non-linearity of the

material behaviour because of the high hydrostatic pressure, i.e. increased loading compresses the pores and micro cracking occurs with the consequence that the pores collapse and the material becomes compacted, which causes the non-linearity. A phase named plastic compaction.

The constitutive relations describe the material behaviour at different pressure states, i.e. a relationship that relates the stress to the strains (ε), strain rates ($\dot{\varepsilon}$), internal energy (*E*) and damage (*D*). In Autodyn this relationship is defined with the RHT model which is defined with yield strength over pressure, where pressure is the mean value of the three principal stresses.

Except the observed result that the dynamic resistance increases with decreased static shear resistance are the results from the parameter study logical and reasonable. The static tensile strength and the *Frate* parameter *D* have been a great support in the calibration process. In the parameter study it was found that by increasing the *D* parameter which control the strain rates, the resistance increased. It was also found that the software Autodyn does not consider the crack softening satisfyingly, which is a fatal error and its effect on the crack pattern should be evaluated in later studies.

The calibration of the model was restricted to only two parameters in the end, the *Frate* parameter *D* and the quotient *fs/fc*. The effect of the static tensile resistance was not used in the calibration by the reason that it is fairly easy to define in tests conducted in a laboratory and should therefore be used according to the characteristic value. Finally, it was found that the values of the parameters presented below give the most convincing results.

$$D = \delta = 0.0328 \qquad fs/fc = 0.17$$

The model after calibration was verified to results from full-scale tests. It works satisfactorily describing the crack pattern on the backside of the member, the so-called outgoing crater. However, on the front side the result is not that convincing, the model gives a crack pattern of the ingoing crater that tends to develop according to the related full-scale experiments but it does not reach full satisfactory status. This could be the cause of that the fracture energy have not been implemented something that could give better results.

5.1   Future studies

In the studies there have been tendencies that the consideration of the strain rates effect works properly but is not approximated fully satisfyingly and could work even better at very high strain rates. The routine describing the effect of the *Frate* may be slightly wrong and need so fourth a deeper evaluation, a work that is left for future studies.

When contact was made with the manufacture of Autodyn about the reason that the fracture energy is not correctly implemented. The manufacture recommended describing the fracture energy by a subroutine. As writing subroutines for Autodyn is outside the limitations of the thesis, the work is left for after comers.

6 References

Attard, M. M. and Setung S. (1996): *Stress-Strain relationship of Confined and Unconfined Concrete.* ACI Materials Journal. Vol. 93, No. 5, 1996, September-October, 432-442 pp.

Erkander, Å. Pettersson, L. (1985): *Betong som splitterskydd.* FOA Report. Försvaret Forskningsanstalt Huvudavdelning 2, FOA Rapport C 20574-(D6)D4, Stockholm, Sweden, 1985, May, 66 pp.

Engström, B. (1994): *Beräkning av betong och murverkskonstruktioner.* Chalmers Reproservice, Publication no. 94:2A and 94:2B, Gothenburg, Sweden, 2001.

Leppänen, J. (2001): *Finita elementanalyser av splitterbelastade betongkonstruktioner.* Chalmers Reproservice, Publication no. 01:1, Gothenburg, Sweden, 2001, 67 pp.

Leppänen, J. (2002): *Dynamic behaviour of concrete structures subjected to blast and fragment impacts.* Licentiate Thesis. Chalmers Reproservice, Publication no. 02:4, Gothenburg, Sweden, 2002, 71 pp.

Janzon, B. (1978): *Grundläggande stridsdelsfysik.* FOA Report. Försvaret Forskningsanstalt Huvudavdelning 2, FOA Rapport C 20261-D4, Stockholm, Sweden, 1978, September, 71-73 pp.

Johansson, M. (2002): *Composite action and confinement effects in tubular steel concrete colums.* Doctoral Thesis. Chalmers Reproservice, Publication no. 02:8, Gothenburg, Sweden, 2002.

Johansson, M. (1998): *Betongens töjningshastighetsberoende och explicit lösningsmetodik.* Doctoral Thesis. Chalmers Reproservice, Publication no. 98:2, Gothenburg, Sweden, 1998, June, 7-15 pp.

Johansson, M. (2000): *Structural behavior in concrete frame corners of civile defence shelters.* Doctoral Thesis. Chalmers Reproservice, Publication no. 00:2, Gothenburg, Sweden, 2000.

Meyers, M. A. (1994): *Dynamic behaviour of materials.* 1994.

Ottosen, N. and Petterson H. (1992): *Introduction to the finite element method.* Redwood Books, Trowbridge, Wiltshire, Great Britain, 1992.

Wiberg, N. and Samuelsson A. (1993): *Byggnadsmekanik Hålfasthetslära.* Studenlitteratur, Lund, Sweden, 1998.

Wiberg, N. and Samuelsson A. (2000): *Finite Elemnt Method - Basics.* Studenlitteratur, Lund, Sweden, 2000.

Zukas, J. A. and Scheffler D. R. (2000): *Practical aspects of numerical simulations of dynamic events: effect of meshing.* International Journal of impact Engineering. Vol. 24, No. 9, 2000, October, 925-945 pp.

Åkesson, M. (1996): *Implementation and application of fracture mechanics models for concrete structures*. Doctoral Thesis. Chalmers Reproservice, Publication no. 96:2, Gothenburg, Sweden, 1996.

Appendix A: Calibration of variables.

C 25:

fcm,cube [Mpa]	35
fck,cube [Mpa]	27
fck,cylinder [Mpa]	21,67

fcm_cyl [Mpa]	29,67		**Gf (formel)**	0,124179606
fctm/fcm	0,078867543		**Gf (tabell)**	0,145
Eci	38300000000,00		**G**	1,47E+10
v	0,30		**fctm [Mpa]**	2,34
			fs [Mpa]	5,3406

Omslutning [Mpa]	Sigma_1_brott [Mpa]	Rest_hållf [Mpa]		**A**	3,2
0	30	0		**N**	0,8
2,1	42,26	15,47		**B**	2,5
4,3	53,2	28,75		**M**	0,7
8,6	71,78	49,03		**p_star_stall**	-5,06E-02
17,2	104,04	82,27			
34	161,68	139,84			

p [Mpa]	q [Mpa]	p_rest [Mpa]
10,00	30,00	0,00
15,49	40,16	6,56
20,60	48,90	12,45
29,66	63,18	22,08
46,15	86,84	38,89
76,56	127,68	69,28

Yield_line and residual strength
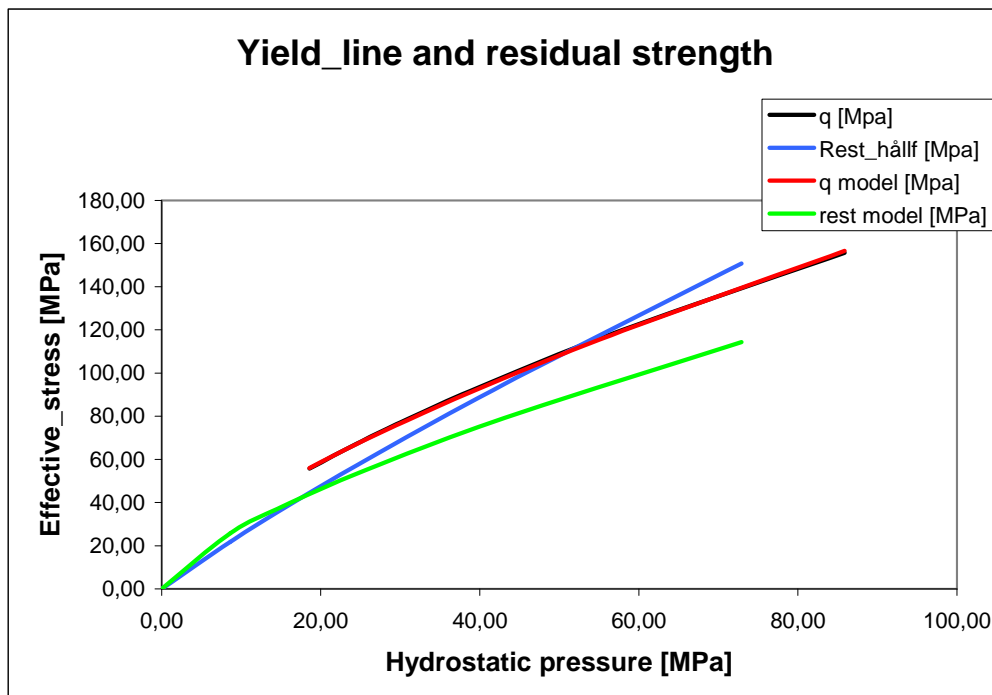
p_star	q model [Mpa]		p_star_rest	rest model [MPa]
0,34	44,48		0,00	0,00
0,52	60,77		0,22	25,78
0,69	75,01		0,42	40,39
1,00	98,74		0,74	60,31
1,56	138,69		1,31	89,64
2,58	205,85		2,34	134,30

C 60:

fcm,cube [Mpa]	65,8	
fck,cube [Mpa]	57,8	
fck,cylinder [Mpa]	47,8	

fcm_cyl [Mpa]	55,80	**Gf (formel)**	0,193228834
fctm/fcm	0,071200717	**Gf (tabell)**	0,145
Eci	3,83E+10	**G**	1,47E+10
v	0,30	**fctm [Mpa]**	3,973
		fs [Mpa]	10,044

Omslutning [Mpa]	Sigma_1_brott [Mpa]	Rest_hållf [Mpa]		
0	55,8	0	**A**	2,05
2,1	69,23	21,76	**N**	0,7
4,3	81,31	36,62	**B**	1,7
8,6	101,57	59,25	**M**	0,7
17,2	135,2	94,86	**p_star_stal**	-2,69E-02
34	189,66	150,71		

p [Mpa]	q [Mpa]	p_rest [Mpa]
18,60	55,80	0,00
24,48	67,13	8,65
29,97	77,01	15,07
39,59	92,97	25,48
56,53	118,00	43,09
85,89	155,66	72,90
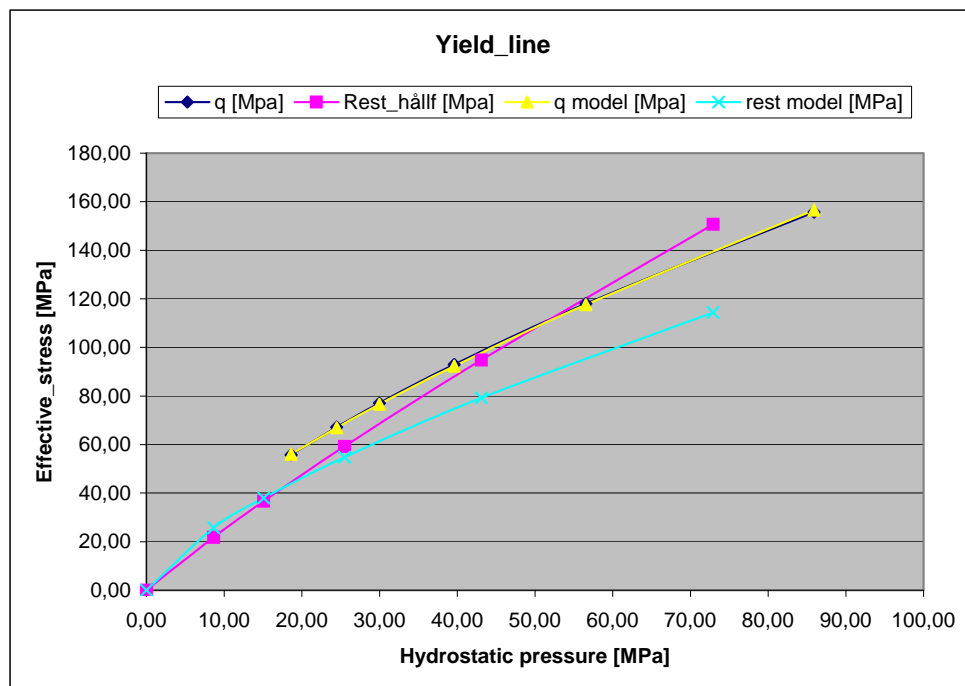
p_star	q model [Mpa]		p_star_rest	rest model [MPa]
0,33		55,97	0,00	0,00
0,44		66,98	0,16	25,73
0,54		76,61	0,27	37,95
0,71		92,33	0,46	54,80
1,01		117,58	0,77	79,16
1,54		156,59	1,31	114,38

Appendix B: Material model steel.

MATERIAL NAME: STEEL

EQUATION OF STATE: Linear

Reference density (g/cm3) : 7.70000E+00

Bulk Modulus (kPa)   : 1.40000E+08

Reference Temperature (K)   : 0.00000E+00

Specific Heat (C.V.) (J/kgK) : 0.00000E+00

STRENGTH MODEL: Vonmises

Shear Modulus (kPa)   : 8.00000E+07

Yield Stress (kPa)   : 9.00000E+05

FAILURE MODEL: None

EROSION MODEL: None

Appendix C: Attard model.

Attard M.M and Setunge S. (1996): Stress-Strain Relationship of Confined and
Unconfined Concrete, ACI Materials Journal

Uniaxial peak stress and strain

$$f_{co} := 31.2$$

$$\varepsilon_{co} := 0.22 \cdot 10^{-2}$$

Youngs Modulus, According to CEB-FIB Model Code 90

$$E_c := 20.7 \cdot 10^3 \qquad\qquad E_{ti} := E_c$$

Tensile strength, Equation 19

$$f_{sp} := 0.32 \cdot \left(f_{co}\right)^{0.67}$$

$$f_t := 0.9 \cdot f_{sp} \qquad\qquad f_t = 2.887$$

Confined peak stress and strain, Equations 17, 18 and 20

$$k_A\left(\sigma_{lat}\right) := 1.25 \cdot \left(1 + 0.062 \cdot \frac{\sigma_{lat}}{f_{co}}\right) \cdot \left(f_{co}\right)^{-0.21}$$

$$f_{ccA}\left(\sigma_{lat}\right) := f_{co} \cdot \left(1 + \frac{\sigma_{lat}}{f_t}\right)^{k_A\left(\sigma_{lat}\right)}$$

$$\varepsilon_{ccA}\left(\sigma_{lat}\right) := \varepsilon_{co} \cdot \left[1 + \left(17 - 0.06 \cdot f_{co}\right) \cdot \left(\frac{\sigma_{lat}}{f_{co}}\right)\right]$$

Stress and strain at point of inflection, Equations 11, 12, 22 and 23

$$\varepsilon_{ic} := \varepsilon_{co} \cdot \left(2.5 - 0.3 \cdot \ln\left(f_{co}\right)\right) \qquad\qquad \text{uniaxial}$$

$$\varepsilon_i\left(\sigma_{lat}\right) := \varepsilon_{ccA}\left(\sigma_{lat}\right) \cdot \left[2 + \frac{\left(\dfrac{\varepsilon_{ic}}{\varepsilon_{co}} - 2\right)}{1.12 \cdot \left(\dfrac{\sigma_{lat}}{f_{co}}\right)^{0.26} + 1}\right] \qquad\qquad \text{confined}$$

$$f_{ic} := f_{co} \cdot \left(1.41 - 0.17 \cdot \ln\left(f_{co}\right)\right) \qquad\qquad \text{uniaxial}$$

$$f_i\left(\sigma_{lat}\right) := f_{ccA}\left(\sigma_{lat}\right) \cdot \left[1 + \frac{\left(\dfrac{f_{ic}}{f_{co}} - 1\right)}{5.06 \cdot \left(\dfrac{\sigma_{lat}}{f_{co}}\right)^{0.57} + 1}\right] \qquad\qquad \text{confined}$$

Stress and strain that correspond to point 2i Equations 24, 25

$$\varepsilon_{2i}\left(\sigma_{lat}\right) := 2 \cdot \varepsilon_i\left(\sigma_{lat}\right) - \varepsilon_{ccA}\left(\sigma_{lat}\right)$$

$$f_{2ic} := f_{co} \cdot \left(1.45 - 0.25 \cdot \ln\left(f_{co}\right)\right) \qquad\qquad \text{uniaxial}$$

$$f_{2i}\left(\sigma_{lat}\right) := f_{ccA}\left(\sigma_{lat}\right) \cdot \left[1 + \frac{\left(\dfrac{f_{2ic}}{f_{co}} - 1\right)}{6.35 \cdot \left(\dfrac{\sigma_{lat}}{f_{co}}\right)^{0.62} + 1}\right] \qquad\qquad \text{confined}$$

$$\varepsilon_{2i}(10) = 0.0311$$

$$f_{2ic} = 18.405$$

$$f_{2i}(10) = 70.95$$

$$E_i\left(\sigma_{lat}\right) := \frac{f_i\left(\sigma_{lat}\right)}{\varepsilon_i\left(\sigma_{lat}\right)} \qquad\qquad E_{2i}\left(\sigma_{lat}\right) := \frac{f_{2i}\left(\sigma_{lat}\right)}{\varepsilon_{2i}\left(\sigma_{lat}\right)}$$

$$E_i(10) = 3.408 \cdot 10^3$$

Parameters A, B, C, D and X: Equation 1, 2, 3 and 4

$$E_{2i}(10) = 2.279 \cdot 10^3$$

$$X\left(\varepsilon_c, \sigma_{lat}\right) := \frac{\varepsilon_c}{\varepsilon_{ccA}\left(\sigma_{lat}\right)}$$

$$A\left(\varepsilon_c, \sigma_{lat}\right) := \left| \begin{array}{l} \dfrac{E_{ti} \cdot \varepsilon_{ccA}\left(\sigma_{lat}\right)}{f_{ccA}\left(\sigma_{lat}\right)} \quad \text{if} \ \varepsilon_c \leq \varepsilon_{ccA}\left(\sigma_{lat}\right) \\[3mm] \left[\dfrac{\left(\varepsilon_{2i}\left(\sigma_{lat}\right) - \varepsilon_i\left(\sigma_{lat}\right)\right)}{\varepsilon_{ccA}\left(\sigma_{lat}\right)}\right]\left[\dfrac{\left(\varepsilon_{2i}\left(\sigma_{lat}\right)\cdot E_i\left(\sigma_{lat}\right)\right)}{\left(f_{ccA}\left(\sigma_{lat}\right) - f_i\left(\sigma_{lat}\right)\right)} - \dfrac{\left(4\cdot\varepsilon_i\left(\sigma_{lat}\right)\cdot E_{2i}\left(\sigma_{lat}\right)\right)}{\left(f_{ccA}\left(\sigma_{lat}\right) - f_{2i}\left(\sigma_{lat}\right)\right)}\right] \ \text{otherwise} \end{array} \right.$$

$$B\left(\varepsilon_c, \sigma_{lat}\right) := \left| \begin{array}{l} \dfrac{\left(A\left(\varepsilon_c, \sigma_{lat}\right) - 1\right)^2}{\left(1 - \dfrac{0.45\cdot f_{co}}{f_{ccA}\left(\sigma_{lat}\right)}\right)} - 1 \quad \text{if} \ \varepsilon_c \leq \varepsilon_{ccA}\left(\sigma_{lat}\right) \\[5mm] \left(\varepsilon_i\left(\sigma_{lat}\right) - \varepsilon_{2i}\left(\sigma_{lat}\right)\right)\cdot\left[\dfrac{E_i\left(\sigma_{lat}\right)}{\left(f_{ccA}\left(\sigma_{lat}\right) - f_i\left(\sigma_{lat}\right)\right)} - \dfrac{4\cdot E_{2i}\left(\sigma_{lat}\right)}{\left(f_{ccA}\left(\sigma_{lat}\right) - f_{2i}\left(\sigma_{lat}\right)\right)}\right] \ \text{otherwise} \end{array} \right.$$

$$C\left(\varepsilon_c, \sigma_{lat}\right) := A\left(\varepsilon_c, \sigma_{lat}\right) - 2$$

$$D\left(\varepsilon_c, \sigma_{lat}\right) := B\left(\varepsilon_c, \sigma_{lat}\right) + 1$$

$$f_{cA}\left(\varepsilon_c, \sigma_{lat}\right) := f_{ccA}\left(\sigma_{lat}\right)\cdot\left[\frac{\left(A\left(\varepsilon_c, \sigma_{lat}\right)\cdot X\left(\varepsilon_c, \sigma_{lat}\right) + B\left(\varepsilon_c, \sigma_{lat}\right)\cdot X\left(\varepsilon_c, \sigma_{lat}\right)^2\right)}{1 + C\left(\varepsilon_c, \sigma_{lat}\right)\cdot X\left(\varepsilon_c, \sigma_{lat}\right) + D\left(\varepsilon_c, \sigma_{lat}\right)\cdot X\left(\varepsilon_c, \sigma_{lat}\right)^2}\right]$$

$$\varepsilon_{ccA}(10) = 0.013$$

$$f_{resid}\left(\varepsilon_c, \sigma_{lat}\right) := f_{ccA}\left(\sigma_{lat}\right)\cdot\frac{B\left(\varepsilon_c, \sigma_{lat}\right)}{B\left(\varepsilon_c, \sigma_{lat}\right) + 1}$$

Legend:
- $f_{cA}\left(\varepsilon_c, 0\right)$
- $f_{cA}\left(\varepsilon_c, 2.1\right)$
- $f_{cA}\left(\varepsilon_c, 4.3\right)$
- $f_{cA}\left(\varepsilon_c, 8.6\right)$
- $f_{cA}\left(\varepsilon_c, 17.2\right)$
- $f_{cA}\left(\varepsilon_c, 200\right)$
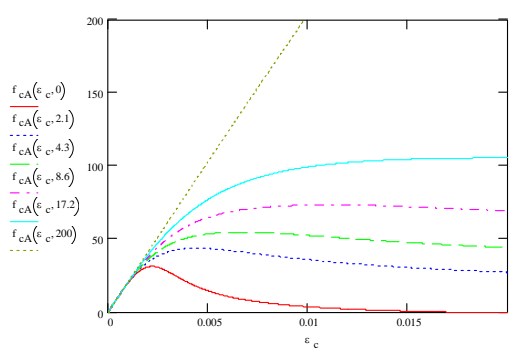
$$\varepsilon_c := 0, 0.0005..\, 0.05 \qquad \sigma_{lat} := 100$$

$$f_{cA}\left(120.01, \sigma_{lat}\right) = 391.85$$

$$f_{resid}\left(100, \sigma_{lat}\right) = 391.809$$

$$f_{ccA}\left(\sigma_{lat}\right) = 419.959$$

$$k_A\left(\sigma_{lat}\right) = 0.728$$

Appendix D: Analysis from calibration of parameters.
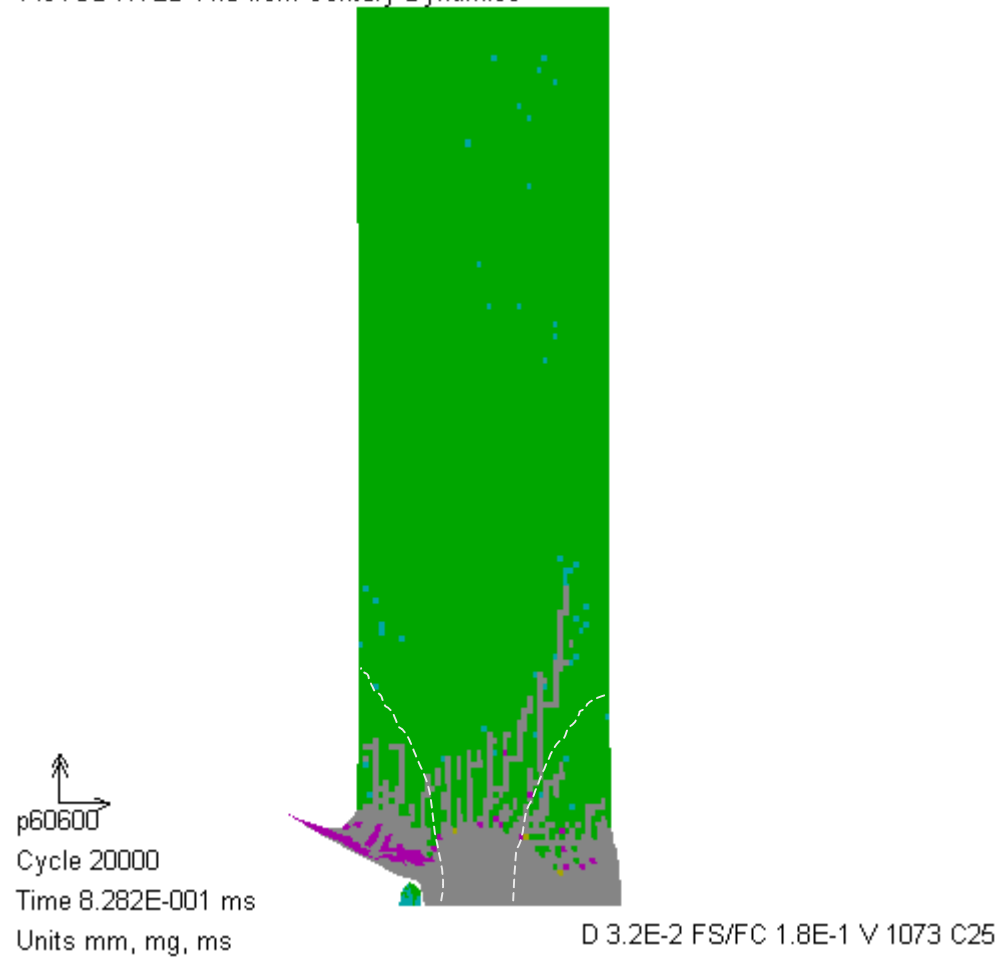

AUTODYN-2D v4.3 from Century Dynamics

p60600
Cycle 20000
Time 8.282E-001 ms
Units mm, mg, ms

D 3.2E-2 FS/FC 1.8E-1 V 1073 C25

Figure 55: Example of calibration analysis with no star status.

AUTODYN-2D v4.3 from Century Dynamics

D:2

p60602

Cycle 20000
Time 7.559E-001 ms
Units mm, mg, ms

D 3.4E-2 FS/FC 0.17 C 25
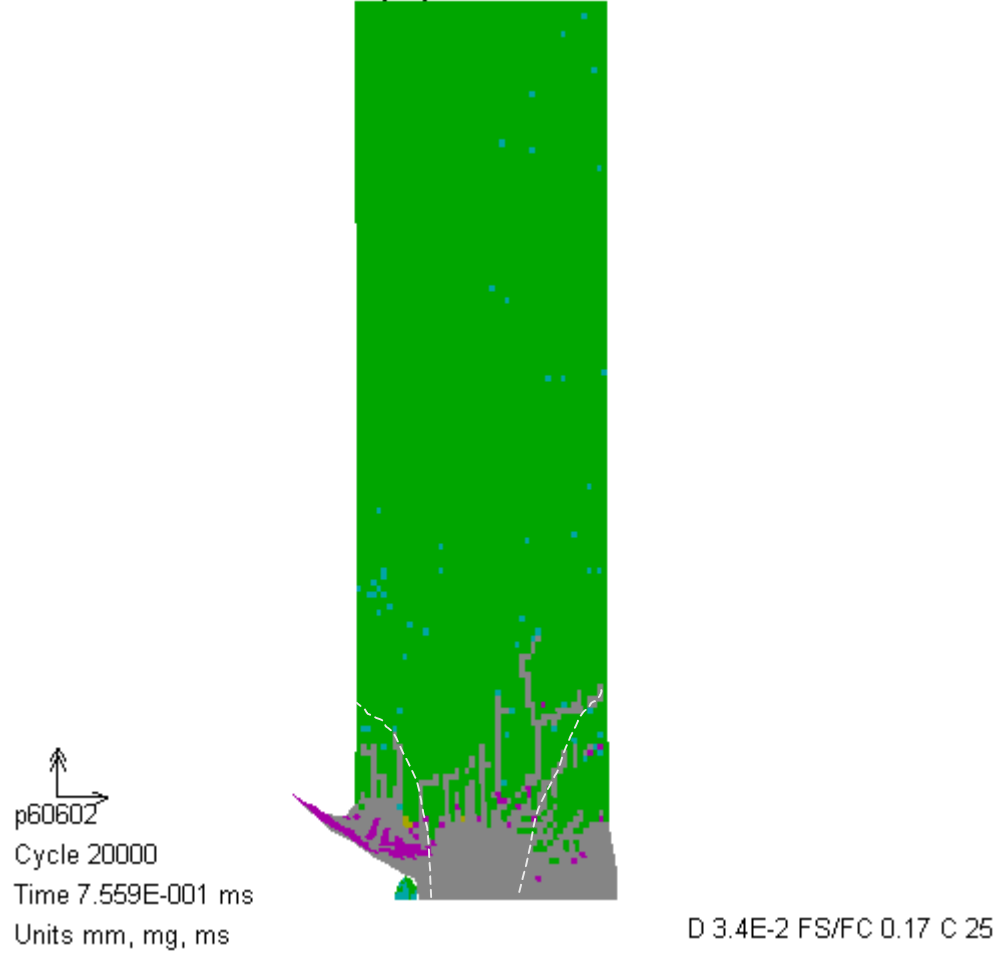
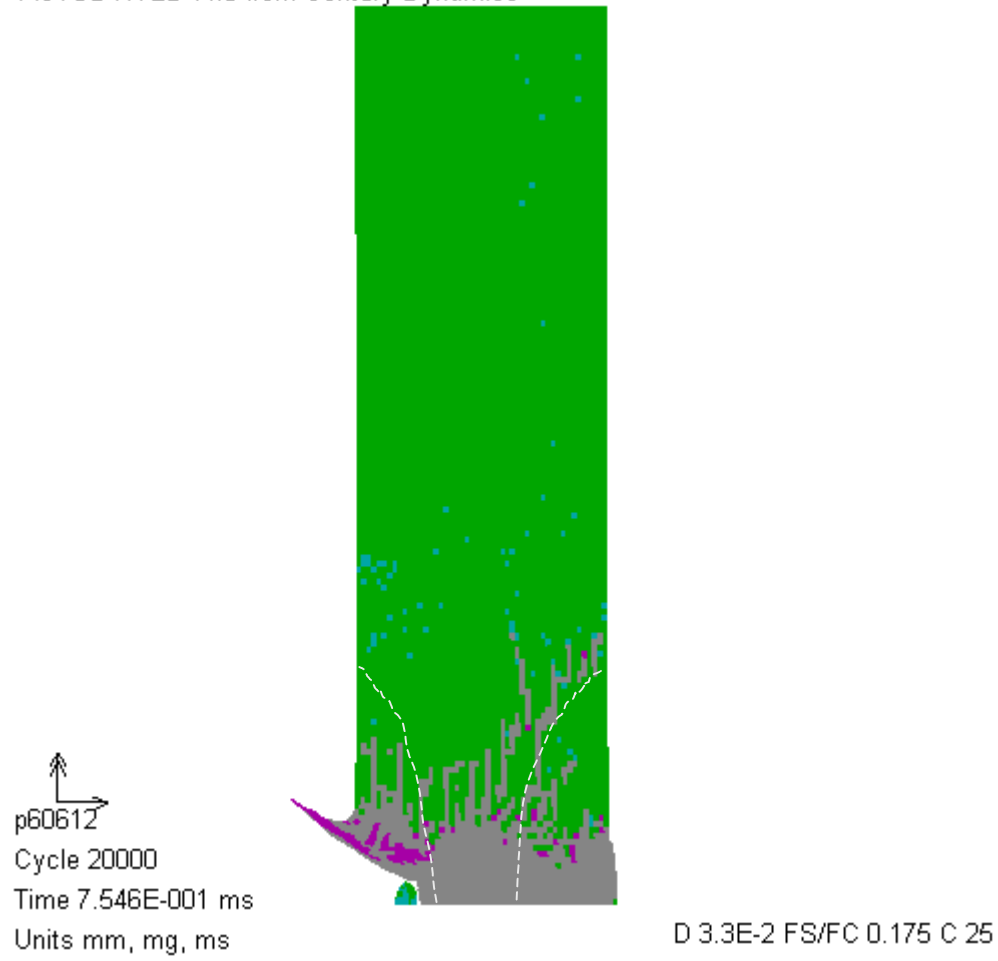*Figure 56: Example of calibration analysis with the status of one star.*

Figure 57: Example of calibration analysis with the status of two stars.